



# LhARA: The Laser-hybrid Accelerator for Radiobiological Applications

G. Aymar<sup>1</sup>, T. Becker<sup>2</sup>, S. Boogert<sup>3</sup>, M. Borghesi<sup>4</sup>, R. Bingham<sup>5,1</sup>,  
 C. Brenner<sup>1</sup>, P.N. Burrows<sup>6</sup>, O.C. Ettliger<sup>7</sup>, T. Dascalu<sup>8</sup>, S. Gibson<sup>3</sup>,  
 T. Greenshaw<sup>9</sup>, S. Gruber<sup>10</sup>, D. Gujral<sup>11</sup>, C. Hardiman<sup>11</sup>, J. Hughes<sup>9</sup>,  
 W.G. Jones<sup>8,20</sup>, K. Kirkby<sup>12</sup>, A. Kurup<sup>8</sup>, J-B. Lagrange<sup>1</sup>, K. Long<sup>8,1</sup>, W. Luk<sup>8</sup>,  
 J. Matheson<sup>1</sup>, P. McKenna<sup>5,14</sup>, R. Mclauchlan<sup>11</sup>, Z. Najmudin<sup>7</sup>, H.T. Lau<sup>8</sup>,  
 J.L. Parsons<sup>9,21</sup>, J. Pasternak<sup>8,1</sup>, J. Pozimski<sup>8,1</sup>, K. Prise<sup>4</sup>, M. Puchalska<sup>13</sup>,  
 P. Ratoff<sup>14</sup>, G. Schettino<sup>15,19</sup>, W. Shields<sup>3</sup>, S. Smith<sup>16</sup>, J. Thomason<sup>1</sup>,  
 S. Towe<sup>17</sup>, P. Weightman<sup>8</sup>, C. Whyte<sup>5</sup>, R. Xiao<sup>18</sup>

<sup>1</sup> STFC Rutherford Appleton Laboratory, Harwell Oxford, Didcot, OX11 0QX, UK

<sup>2</sup> Maxeler Technologies Limited, 3 Hammersmith Grove, London W6 0ND, UK

<sup>3</sup> John Adams Institute for Accelerator Science, Royal Holloway, University of London, Egham, Surrey, TW20 0EX, UK

<sup>4</sup> Queens University Belfast, University Road, Belfast, BT7 1NN, Northern Ireland, UK

<sup>5</sup> Department of Physics, SUPA, University of Strathclyde, 16 Richmond Street, Glasgow, G1 1XQ, UK

<sup>6</sup> John Adams Institute for Accelerator Science, University of Oxford, Denys Wilkinson Building, Keble Road, Oxford OX1 3RH, UK

<sup>7</sup> John Adams Institute for Accelerator Science, Imperial College London, Exhibition Road, London, SW7 2AZ, UK

<sup>8</sup> Imperial College London, Exhibition Road, London, SW7 2AZ, UK

<sup>9</sup> University of Liverpool, Liverpool L3 9TA, UK

<sup>10</sup> Christian Doppler Laboratory for Medical Radiation Research for Radiation Oncology, Medical University of Vienna, Spitalgasse 23, 1090 Vienna, Austria

<sup>11</sup> Imperial College NHS Healthcare Trust, The Bays, South Wharf Road, St Mary's Hospital, London W2 1NY, UK

<sup>12</sup> University of Manchester, Oxford Road, Manchester, M13 9PL, UK

<sup>13</sup> Technische Universität Wien, Atomintitut, Stadionallee 2, 1020 Vienna, Austria

<sup>14</sup> Cockcroft Institute, Daresbury Laboratory, Sci-Tech Daresbury, Daresbury, Warrington, WA4 4AD, UK

<sup>15</sup> National Physical Laboratory, Hampton Road, Teddington, Middlesex, TW11 0LW, UK

<sup>16</sup> STFC Daresbury Laboratory, Daresbury, Cheshire, WA4 4AD, UK

<sup>17</sup> Leo Cancer Care, Broadview, Windmill Hill, Hailsham, East Sussex, BN27 4RY, UK

<sup>18</sup> Corerain Technologies, 14F, Changfu Jinmao Building (CFC), Trade-free Zone, Futian District, Shenzhen, Guangdong, China

<sup>19</sup> University of Surrey, 388 Stag Hill, Guilford, GU2 7XH, UK

<sup>20</sup> Imperial Patient and Public Involvement Group (IPPIG), Imperial College London, Exhibition Road, London, SW7 2AZ, UK

<sup>21</sup> The Clatterbridge Cancer Centre, Bebington, CH63 4JY, UK

This is a provisional file, not the final typeset article

Correspondence:

A. Kurup

a.kurup@imperial.ac.uk

## 2 ABSTRACT

3 The 'Laser-hybrid Accelerator for Radiobiological Applications', LhARA, is conceived as a novel,  
4 uniquely-flexible facility dedicated to the study of radiobiology. The technologies demonstrated  
5 in LhARA, which have wide application, will be developed to allow particle-beam therapy to be  
6 delivered in a completely new regime, combining a variety of ion species in a single treatment  
7 fraction and exploiting ultra-high dose rates. LhARA will be a hybrid accelerator system in which  
8 laser interactions drive the creation of a large flux of protons or light ions that are captured using  
9 a plasma (Gabor) lens and formed into a beam. The laser-driven source allows protons and ions  
10 to be captured at energies significantly above those that pertain in conventional facilities, thus  
11 evading the current space-charge limit on the instantaneous dose rate that can be delivered.  
12 The laser-hybrid approach, therefore, will allow the vast "terra incognita" of the radiobiology  
13 that determines the response of tissue to ionising radiation to be studied with protons and light  
14 ions using a wide variety of time structures, spectral distributions, and spatial configurations at  
15 instantaneous dose rates up to and significantly beyond the ultra-high dose-rate 'FLASH' regime.

16 It is proposed that LhARA be developed in two stages. In the first stage, a programme of *in*  
17 *vitro* radiobiology will be served with proton beams with energies between 10 MeV and 15 MeV.  
18 In stage two, the beam will be accelerated using a fixed-field accelerator (FFA). This will allow  
19 experiments to be carried out *in vitro* and *in vivo* with proton beam energies of up to 127 MeV.  
20 In addition, ion beams with energies up to 33.4 MeV per nucleon will be available for *in vitro*  
21 and *in vivo* experiments. This paper presents the conceptual design for LhARA and the R&D  
22 programme by which the LhARA consortium seeks to establish the facility.

## 23 LAY SUMMARY

24 It is well established that radiation therapy (RT) is an effective treatment for many types of cancer.  
25 Most treatments are delivered by machines that accelerate electrons which are then used to  
26 produce a beam of high-energy photons (X-rays) which are directed at a tumour to kill cancer  
27 cells. However, healthy tissue anywhere in the path of the photon beam is also irradiated and so  
28 can be damaged. Modern X-ray therapy is able to reduce this damage by using several beams at  
29 different angles.

30 Recent years have seen the use of a new type of machine in which protons are accelerated to  
31 produce proton beams (rather than photon beams) which are directed at a tumour. These proton  
32 beams can be arranged to deposit almost all of their energy in a small volume within a tumour so  
33 they cause little damage to healthy tissue; a major advantage over photon beams. But proton  
34 machines are large and expensive, so there is a need for the development of proton machines  
35 that are smaller, cheaper and more flexible in how they can be used.

36 The LhARA project is aimed at the development of such proton machines using a new approach  
37 based on high powered lasers. Such new machines could also make it easier to deliver the dose  
38 in very short high-intensity pulses and as a group of micro-beams—exciting recent research has  
39 shown that this brings improved effectiveness in killing cancer cells while sparing healthy tissue.  
40 The technology to be proved in LhARA should enable a course of RT to be delivered in days  
41 rather than weeks and should be more effective.

42 Scientifically, there is a need to understand much better the basic processes by which radiation  
43 interacts with biological matter to kill cancer cells—the investigation of these processes involves  
44 physics as well as biology. Thus the most important aim of LhARA is to pursue this radiobiological

45 research in new regimes and from this to develop better treatments. LhARA will also pursue  
46 technological research into laser-hybrid accelerators.

47 **Keywords:** Radiobiology, Novel acceleration, Proton beam therapy, Ion beam therapy, Laser-driven acceleration, Plasma lens, Fixed  
48 field alternating gradient acceleration

## 1 INTRODUCTION

49 Cancer is the second most common cause of death globally [The World Health Organisation (2020)]. In  
50 2018, 18.1 million new cancer cases were diagnosed, 9.6 million people died of cancer-related disease, and  
51 43.8 million people were living with cancer [Bray et al. (2018); Fitzmaurice et al. (2018)]. It is estimated  
52 that 26.9 million life-years could be saved in low- and middle-income countries if radiotherapy capacity  
53 could be scaled up [Atun et al. (2015)]. Novel techniques incorporated in facilities that are at once robust,  
54 automated, efficient, and cost-effective are required to deliver the required scale-up in provision.

55 Radiation therapy (RT), a cornerstone of cancer treatment, is used in over 50% of cancer patients [Datta  
56 et al. (2019)]. The most frequently used types of radiotherapy employ photon or electron beams with  
57 MeV-scale energies. Proton and ion beams offer substantial advantages over X-rays because the bulk of  
58 the beam energy is deposited in the Bragg peak. This allows dose to be conformed to the tumour while  
59 sparing healthy tissue and organs at risk. The benefits of proton and ion-beam therapy (PBT) are widely  
60 recognised. PBT today is routinely delivered in fractions of  $\sim 2$  Gy per day over several weeks; each  
61 fraction being delivered at a rate of  $\lesssim 5$  Gy/minute deposited uniformly over the target treatment volume.  
62 Exciting evidence of novel RT delivery has recently been reported, including delivery of doses at ultra-high  
63 dose-rate,  $\gtrsim 40$  Gy/s (“FLASH” RT) or utilising multiple micro-beams with diameter less than 1 mm  
64 distributed over a grid with inter-beam spacing. However, the radiobiological mechanisms by which the  
65 therapeutic benefit is generated using these approaches are not entirely understood.

66 LhARA, the Laser-hybrid Accelerator for Radiobiological Applications, is conceived as the new, highly  
67 flexible, source of radiation that is required to explore the vast “terra incognita” of the mechanisms by  
68 which the biological response to ionising radiation is determined by the physical characteristics of the  
69 beam. A high-power pulsed laser will be used to drive the creation of a large flux of protons or light ions  
70 which are captured and formed into a beam by strong-focusing plasma lenses. The plasma (Gabor) lenses  
71 provide the same focusing strength as high-field solenoids at a fraction of the cost. Rapid acceleration  
72 will be performed using a fixed-field alternating-gradient accelerator (FFA) thereby preserving the unique  
73 flexibility in the time, energy, and spatial structure of the beam afforded by the laser-driven source.

74 We propose that LhARA be developed in two stages. In the first stage, the laser-driven beam, captured  
75 and transported using plasma lenses and bending magnets, will serve a programme of *in vitro* radiobiology  
76 with proton beams of energy of up to 15 MeV. In stage two, the beam will be accelerated using an FFA. This  
77 will allow experiments to be carried out *in vitro* and *in vivo* with proton-beam energies of up to 127 MeV.  
78 Ion beams (including  $C^{6+}$ ) with energies up to 33.4 MeV per nucleon will also be available.

79 The laser pulse that initiates the production of protons or ions at LhARA may be triggered at a repetition  
80 rate of up to 10 Hz. The time structure of the beam may therefore be varied to interrupt the chemical  
81 and biological pathways that determine the biological response to ionising radiation with 10 ns to 40 ns  
82 long proton or ion bunches repeated at intervals as small as 100 ms. The technologies chosen to capture,  
83 transport, and accelerate the beam in LhARA have been made so that this unique capability is preserved.  
84 The LhARA beam may be used to deliver an almost uniform dose distribution over a circular area with  
85 a maximum diameter of between 1 cm and 3 cm. Alternatively the beam can be focused to a spot with  
86 diameter of  $\sim 1$  mm.

87 The technologies demonstrated in LhARA have the potential to be developed to make “best in class”  
88 treatments available to the many. The laser-hybrid approach will allow radiobiological studies and eventually  
89 radiotherapy to be carried out in completely new regimes, delivering a variety of ion species in a broad

90 range of time structures, spectral distributions, and spatial configurations at instantaneous dose rates up to  
91 and potentially significantly beyond the current ultra-high dose-rate “FLASH” regime.

92 The LhARA consortium is the multidisciplinary collaboration of clinical oncologists, medical and  
93 academic physicists, biologists, engineers, and industrialists required to deliver such a transformative  
94 particle-beam system. With its “pre Conceptual Design Report” (pre-CDR) [The LhARA consortium  
95 (2020)] the consortium lays out its concept for LhARA, its potential to serve a ground-breaking programme  
96 of radiobiology, and the technological advances that will be made in its execution. The work presented in  
97 the LhARA pre-CDR lays the foundations for the development of full conceptual and technical designs  
98 for the facility. The pre-CDR also contains a description of the R&D that is required to demonstrate the  
99 feasibility of critical components and systems. This paper presents a summary of the contents of the  
100 pre-CDR and lays out the vision of the consortium.

101

## 2 MOTIVATION

102 RT delivered using protons and ions, particle-beam therapy (PBT), has the potential to overcome some  
103 of the fundamental limitation of X-rays in cancer treatment through targeted delivery of the radiation  
104 dose [Loeffler and Durante (2013)]. The Particle Therapy Co-Operative Group (PTCOG) currently lists  
105 90 proton therapy facilities and 12 carbon ion therapy facilities, located predominantly in high-income  
106 countries [PTCOG (2020)]. Low- and middle-income countries (LMIC) are relatively poorly served, indeed  
107 nearly 70% of cancer patients globally do not have access to RT [Datta et al. (2019)]. Novel RT techniques  
108 incorporated in facilities that are robust, automated, efficient, and cost-effective are therefore required to  
109 deliver the necessary scale-up in provision. This presents both a challenge and an opportunity; developing  
110 the necessary techniques and scaling up RT provision will require significant investment but will also  
111 create new markets, drive economic growth through new skills and technologies and deliver impact through  
112 improvements in health and well-being.

### 113 **The case for a systematic study of the radiobiology of proton and ion beams**

114 The efficacy of proton and ion beams is characterised by their relative biological effectiveness (RBE) in  
115 comparison to reference photon beams. The treatment-planning software that is in use in the clinic today  
116 assumes an RBE value for protons of 1.1 [Paganetti and van Luijk (2013)], meaning that a lower dose of  
117 protons is needed to produce the same therapeutic effect that would be obtained using X-rays. However,  
118 the rapid rise in the linear energy transfer (LET) at the Bragg peak leads to significant uncertainties in the  
119 RBE. Furthermore, it is known that RBE depends strongly on many factors, including particle energy, dose,  
120 dose rate, the degree of hypoxia, and tissue type [Paganetti (2014)]. Indeed, RBE values from 1.1 to over 3  
121 have been derived from *in vitro* clonogenic-survival assay data following proton irradiation of cultured  
122 cell lines derived from different tumours [Paganetti (2014); Chaudhary et al. (2014); Wilkens and Oelfke  
123 (2004)]. RBE values of  $\sim 3$  are accepted for high-LET carbon-ion irradiation, although higher values have  
124 been reported [Karger and Peschke (2017)]. RBE uncertainties for carbon and other ion species are at  
125 least as large as they are for protons. These uncertainties can lead to an incorrect estimation of the dose  
126 required to treat a particular tumour. Overestimation can lead to risk of damage to healthy tissue, while an  
127 underestimate can lead to the tumour not being treated sufficiently for it to be eradicated.

128 Given that the therapeutic of RT is largely caused by irreparable damage to the cell’s DNA, differences  
129 in RBE can also affect the spectrum of DNA damage induced within tumour cells. Larger RBE values,  
130 corresponding to higher LET, can cause increases in the frequency and complexity of DNA damage,  
131 particularly DNA double-strand breaks (DSB) and complex DNA damage (CDD) where multiple DNA

132 lesions are induced in close proximity [Vitti and Parsons (2019); Carter et al. (2018)]. These DNA lesions  
133 are a major contributor to radiation-induced cell death as they represent a significant barrier to the cellular  
134 DNA-repair machinery [Vitti and Parsons (2019)]. However, a number of other biological factors contribute  
135 to varying RBE in specific tumours, including the intrinsic radiosensitivity of the tissue, the level of  
136 oxygenation (hypoxia), the growth and repopulation characteristics, and the associated tumour micro-  
137 environment. Consequently, there is still significant uncertainty in the precise radiobiological mechanisms  
138 that arise and how these mechanisms are affected by PBT. Detailed systematic studies of the biophysical  
139 effects of the interaction of protons and ions, under different physical conditions, with different tissue  
140 types will provide important information on RBE variation and could enable enhanced patient treatment-  
141 planning algorithms to be devised. In addition, studies examining the impact of combination therapies  
142 with PBT (e.g. targeting the DNA damage response, hypoxia signalling mechanisms and also the tumour  
143 micro-environment) are currently sparse; performing these studies will therefore provide input vital to the  
144 development of future personalised patient-therapy strategies using PBT.

#### 145 **The case for novel beams for radiobiology**

146 PBT delivery to date has been restricted to a small number of beam characteristics. In a typical treatment  
147 regimen the therapeutic dose is provided in a series of daily sessions delivered over a period of several  
148 weeks. However, recent evidence has demonstrated that when the dose is delivered at ultra-high dose rates  
149 ( $> 40$  Gy/s) “FLASH” RT, there is significant normal tissue sparing [Favaudon et al. (2014); Vozenin  
150 et al. (2019)]. Indeed, significantly reduced lung fibrosis in mice, skin toxicity in mini-pigs, and reduced  
151 side-effects in cats with nasal squamous-cell carcinoma have been observed which is currently thought  
152 to be mediated via local oxygen depletion (add Wilson et al., 2020). In fact, the first patient with CD30+  
153 T-cell cutaneous lymphoma has been shown to be safely treated with electrons delivered at FLASH dose  
154 rates (add Bourhis et al., 2019). In addition, therapeutic benefit has been demonstrated with the use of  
155 multiple micro-beams with diameter of less than 1 mm distributed over a grid with inter-beam spacing of  
156 3 mm [Prezado et al. (2017)]. However, there is still significant uncertainty regarding the thresholds and the  
157 radiobiological mechanisms by which therapeutic benefit is generated in FLASH and micro-beam therapy,  
158 which require extensive further study both *in vitro* and in appropriate *in vivo* models.

159 LhARA is designed to be a highly flexible source delivering the temporal, spectral, and spatial beam  
160 structures that are required to elucidate the mechanisms by which the biological response to ionising  
161 radiation is determined by the physical characteristics of the beam, including FLASH and micro-beam  
162 effects. These comprehensive studies are not currently possible at clinical RT facilities. Thus the LhARA  
163 facility will provide greater accessibility to stable ion beams, enable different temporal fractionation  
164 schemes, and deliver reliable and reproducible biological data with fewer constraints than at current clinical  
165 centres. The availability of several ion beams (from protons to heavier ions) within the same facility will  
166 provide further flexibility, and the ability to perform direct radiobiological comparisons of the effects of  
167 different charged particles at different energies and dose rates, and to perform mechanistic studies (e.g.  
168 examining the oxygen depletion hypothesis for FLASH) will be truly unique. In addition, LhARA will  
169 enable exhaustive evaluations of RBE using more complex end-points (e.g. angiogenesis and inflammation)  
170 in addition to routine survival measurements. The ability to evaluate charged particles in conjunction  
171 with other therapies (immunotherapy and chemotherapy), and of performing *in vivo* experiments with the  
172 appropriate animal models is a huge advantage given the current lack of evidence in these areas. LhARA  
173 therefore has the potential to yield the accumulation of radiobiological data that can drive a significant  
174 change in current clinical practice. The simulations of LhARA that are described in this document have  
175 been used to estimate the dose delivered as a function of energy for protons and carbon ions. Details of  
176 the simulations can be found in sections 3.3 and 3.4. The simulations show instantaneous particle rates on

177 the order of  $10^9$  particles per shot can be achieved, corresponding to average dose rates up to  $\gtrsim 120$  Gy/s  
178 for protons and  $\gtrsim 700$  Gy/s for carbon ions. These estimates are based on the baseline specifications for  
179 LhARA.

### 180 **Laser-hybrid beams for radiobiology and clinical application**

181 High-power lasers have been proposed as an alternative to conventional proton and carbon-ion facilities  
182 for radiotherapy [Bulanov et al. (2002); Fourkal et al. (2003); Malka et al. (2004)]. The capability of  
183 laser-driven ion beams to generate protons and high-LET carbon ions at FLASH dose rates is a significant  
184 step forward for the provision of local tumour control whilst sparing normal tissue. High-power lasers  
185 have also been proposed to serve as the basis of electron, proton and ion-beams for radiobiology [Kraft  
186 et al. (2010); Fiorini et al. (2011); Doria et al. (2012); Zeil et al. (2013); Masood et al. (2014); Zlobinskaya  
187 et al. (2014)]. More recent projects (e.g. A-SAIL [A-SAIL Project (2020)], ELI [Cirrone et al. (2013)] and  
188 SCAPA [Wiggins et al. (2019)]) will also investigate radiobiological effects using laser-driven ion beams.  
189 These studies will also address various technological issues [Manti et al. (2017); Romano et al. (2016a);  
190 Masood et al. (2017); Chaudhary et al. (2017); Margarone et al. (2018)].

191 The LhARA collaboration's concept is to exploit a laser to drive the creation of a large flux of protons  
192 or light ions which are captured and formed into a beam by strong-focusing plasma lenses. Protons and  
193 ions at conventional facilities are captured at energies of several tens of keV. At such low energies the  
194 mutual repulsion of the particles, the "space-charge effect", limits the maximum instantaneous dose rate.  
195 The laser-driven source allows protons and ions to be captured at energies significantly above those that  
196 pertain in conventional facilities, thus evading the current space-charge limit on the instantaneous dose  
197 rate that can be delivered. Rapid acceleration will be performed using a fixed-field alternating-gradient  
198 accelerator (FFA) thereby preserving the unique flexibility in the time, energy, and spatial structure of  
199 the beam afforded by the laser-driven source. Modern lasers are capable of delivering a Joule of energy  
200 in pulses that are tens of femtoseconds in length at repetition rates of  $\gtrsim 10$  Hz. Laser-driven ion sources  
201 create beams that are highly divergent, have a large energy spread, and an intensity that can vary by up to  
202 25% pulse-to-pulse [Dover et al. (2020)]. These issues are addressed in the conceptual design through the  
203 use of plasma lenses to provide strong focusing and to allow energy selection. In addition, sophisticated  
204 instrumentation will be used in a fast feedback-and-control system to ensure that the dose delivered is both  
205 accurate and reproducible. This approach will allow produce multiple ion species, from proton to carbon,  
206 to be produced from a single laser by varying the target foil and particle-capture optics.

207 The LhARA consortium's vision is that LhARA will prove the principle of the novel technologies required  
208 for the development of future therapy facilities. The legacy of the LhARA programme will therefore be:

- 209 • A unique facility dedicated to the development of a deep understanding of the radiobiology of proton  
210 and ion beams; and
- 211 • The demonstration in operation of technologies that will allow PBT to be delivered in completely new  
212 regimes.

213

## 3 THE LHARA FACILITY

214 The LhARA facility, shown schematically in figure 1, has been designed to serve two end stations for  
215 *in vitro* radiobiology and one end station for *in vivo* studies. The principle components of the LhARA  
216 accelerator are: the laser-driven proton and ion source; the matching and energy selection section; beam

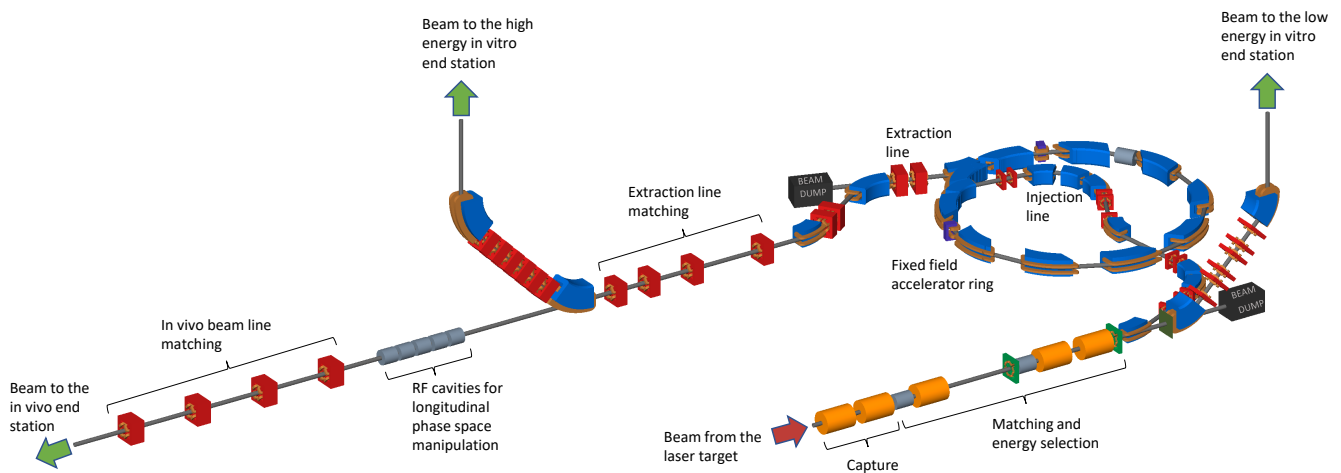


**Figure 1.** Schematic diagram of the LhARA beam lines. The particle flux from the laser-driven source is shown by the red arrow. The ‘Capture’ section is followed by the ‘Matching and energy selection’ section. The beam is then directed either into the 90° bend that takes it to the low-energy *in vitro* end station, towards the FFA injection line, or to the low-energy beam dump. Post acceleration is performed using the FFA on extraction from which the beam is directed either to the high-energy *in vitro* end station, the *in vivo* end station, or the high-energy beam dump. Gabor lenses are shown as the orange cylinders, RF cavities as grey cylinders, quadrupole magnets as red squares, octopole magnets as green discs, and dipole magnets are shown in blue. The beam-line elements are discussed in section 3.

217 delivery to the low-energy *in vitro* end station; the low-energy abort line; the injection line for the fixed-  
 218 field alternating-gradient accelerator (FFA); the FFA; the extraction line; the high-energy abort line; beam  
 219 delivery to the high-energy *in vitro* end station; and the transfer line to the *in vivo* end station. Proton beams  
 220 with energies of between 12 MeV and 15 MeV will be delivered directly from the laser-driven source to  
 221 the low-energy *in vitro* end station via a transfer line. The high-energy *in vitro* end station and the *in vivo*  
 222 end station will be served by proton beams with energy between 15 MeV and 127 MeV and by ion beams,  
 223 including  $C^{6+}$  with energies up to 33.4 MeV/u. This configuration makes it natural to propose that LhARA  
 224 be constructed in two stages; Stage 1 providing beam to the low-energy *in vitro* end station and Stage 2  
 225 delivering the full functionality of the facility. The development of LhARA Stage 1 will include machine  
 226 performance and optimisation studies designed to allow *in vitro* experiments to begin as soon as possible.

227 The design parameters for the various components of LhARA are given in tables 1 and 2. The design of  
 228 the LhARA facility is described in the sections that follow.

229

### 230 3.1 Laser-driven proton and ion source

231 Laser-driven ions have been posited as a source for radiobiological studies for a number of years [Kraft  
 232 et al. (2010); Yogo et al. (2011); Bin et al. (2012)]. Until now, the achievable ion energies, energy  
 233 spreads, and reproducibility of such beams have meant that such sources are not suitable for a full  
 234 radiobiological laboratory setting. While a number of cell irradiation experiments have been conducted  
 235 with laser-accelerated ions [Doria et al. (2012); Zeil et al. (2013); Pommarel et al. (2017); Manti et al.  
 236 (2017)], these have been limited in scope to a single-shot configuration. In addition, most of these  
 237 experiments have been performed on high-power laser facilities with rapidly shifting priorities, where the  
 238 time to install dedicated diagnostic systems has not been available. A beam line to provide ion-driven  
 239 beams for multi-disciplinary applications, ELIMAIA (ELI Multidisciplinary Applications of laser-Ion  
 240 Acceleration) is being brought into operation at the Extreme Light Infrastructure (ELI) Cirrone et al. (2020);

**Table 1.** Design parameters of the components of the LhARA facility. The parameter table is provided in a number of sections. This section contains parameters for the Laser-driven proton and ion source, the Proton and ion capture section, and the Stage 1 beam transport section.

Parameter	Value or range	Unit
<b>Laser driven proton and ion source</b>		
Laser power	100	TW
Laser Energy	2.5	J
Laser pulse length	25	fs
Laser rep. rate	10	Hz
Required maximum proton energy	15	MeV
<b>Proton and ion capture</b>		
Beam divergence to be captured	50	mrad
Gabor lens effective length	0.857	m
Gabor lens length (end-flange to end-flange)	1.157	m
Gabor lens cathode radius	0.0365	m
Gabor lens maximum voltage	65	kV
Number of Gabor lenses	2	
Alternative technology: solenoid length	1.157	m
Alternative technology: solenoid max field strength	1.3	T
<b>Stage 1 beam transport: matching &amp; energy selection, beam delivery to low-energy end station</b>		
Number of Gabor lenses	3	
Number of re-bunching cavities	2	
Number of collimators for energy selection	1	
Arc bending angle	90	Degrees
Number of bending magnets	2	
Number of quadrupoles in the arc	6	
Alternative technology: solenoid length	1.157	m
Alternative technology: solenoid max field strength (to serve the injection line to the Stage 2)	0.8 (1.4)	T

241 Schillaci et al. (2019). This beam line will include the “ELI MEDical and multidisciplinary applications”  
 242 (ELIMED) beam line which will allow radiobiological investigations to be carried out Cirrone et al. (2016);  
 243 Romano et al. (2016b); Milluzzo et al. (2017); Pipek et al. (2017); Milluzzo et al. (2018); Cirrone et al.  
 244 (2020); ?. LhARA is distinguished from this facility in that the energy at which the beam will be captured  
 245 has been chosen to maximise the shot-to-shot stability of the particle flux. As a result, LhARA has the  
 246 potential to become a unique, state-of-the-art system, able to explore the radiobiological benefits of a  
 247 laser-accelerated ion source.

248 A novel solution for ion-acceleration is to use a compact, flexible laser-driven source coupled to a  
 249 state-of-the-art beam-transport line. This allows an accelerating gradient of  $\gtrsim 10$  GV/m to be exploited at  
 250 the laser-driven source. We propose to operate in a laser-driven sheath-acceleration regime [Clark et al.  
 251 (2000a); Snavely et al. (2000); Daido et al. (2012)] for ion generation. An intense, short laser pulse will  
 252 be focused onto a target. The intense electric field generated on the front surface of the target accelerates  
 253 the surface electrons, driving them into the material. Electrons which gain sufficient energy traverse the  
 254 target, ionising the material as they go. A strong space-charge electric field, the ‘sheath’, is created as the  
 255 accelerated electrons exit the rear surface of the target. This field in turn accelerates surface-contaminant  
 256 ions. The sheath-acceleration scheme has been shown to produce ion energies greater than 40 MeV/u at the  
 257 highest laser intensities. The maximum proton energy ( $E_p$ ) scales with laser intensity ( $I$ ) as,  $E_p \propto I^{\frac{1}{2}}$ . The

**Table 2.** Design parameters of the components of the LhARA facility. The parameter table is provided in a number of sections. This section contains parameters for the Stage 2 beam transport and the *in vitro* and *in vivo* end stations.

Parameter	Value or range	Unit
<b>Stage 2 beam transport:</b> FFA, transfer line, beam delivery to high-energy end stations		
Number of bending magnets in the injection line	7	
Number of quadrupoles in the injection line	10	
FFA: Machine type	single spiral scaling FFA	
FFA: Extraction energy	15–127	MeV
FFA: Number of cells	10	
FFA: Orbit $R_{\min}$	2.92	m
FFA: Orbit $R_{\max}$	3.48	m
FFA: Orbit excursion	0.56	m
FFA: External R	4	m
FFA: Number of RF cavities	2	
FFA: RF frequency	1.46–6.48	MHz
FFA: harmonic number	1, 2 or 4	
FFA: RF voltage (for 2 cavities)	4	kV
FFA: spiral angle	48.7	Degrees
FFA: Max B field	1.4	T
FFA: k	5.33	
FFA: Magnet packing factor	0.34	
FFA: Magnet opening angle	12.24	degrees
FFA: Magnet gap	0.047	m
FFA: Ring tune (x,y)	(2.83,1.22)	
FFA: $\gamma_T$	2.516	
FFA: Number of kickers	2	
FFA: Number of septa	2	
Number of bending magnets in the extraction line	2	
Number of quadrupoles in the extraction line	8	
Vertical arc bending angle	90	Degrees
Number of bending magnets in the vertical arc	2	
Number of quadrupoles in the vertical arc	6	
Number of cavities for longitudinal phase space manipulation	5	
Number of quadrupoles in the <i>in vivo</i> beam line	4	
<b><i>In vitro</i> biological end stations</b>		
Maximum input beam diameter	1-3	cm
Beam energy spread (full width)	Low-energy end station: $\leq 4$ High-energy end station: $\leq 1$	% %
Input beam uniformity	$< 5$	%
Scintillating fibre layer thickness	0.25	mm
Air gap length	5	mm
Cell culture plate thickness	1.3	mm
Cell layer thickness	0.03	mm
Number of end stations	2	
<b><i>In vivo</i> biological end station</b>		
Maximum input beam diameter	1-3	cm
Beam energy spread (full width)	$\leq 1$	%
Input beam uniformity	$< 5$	%
Beam options	Spot-scanning, passive scattering, micro-beam	

258 laser required to deliver a significant proton flux at 15 MeV can be compact, relatively inexpensive, and is  
259 commercially available.

260 The distribution of proton and ion energies observed in laser-driven beams exhibits a sharp cut off at  
261 the maximum energy and, historically, the flux of laser-accelerated ion beams has varied significantly  
262 shot-to-shot. To reduce the impact of the shot-to-shot variations the choice has been made to select particles  
263 from the plateau of the two-temperature energy spectrum of the laser-accelerated ion beam Clark et al.  
264 (2000b); Passoni et al. (2010). This choice should enhance ion-beam stability and allow reproducible  
265 measurements to be carried out at ultra-high dose rates using a small number of fractions. To create the flux  
266 required in the plateau region it is proposed that a 100 TW laser system is used. A number of commercial  
267 lasers are available that are capable of delivering  $> 2.5$  J in pulses of duration  $< 25$  fs, at 10 Hz with  
268 contrast better than  $10^{10} : 1$ . Shot-to-shot stability of  $< 1\%$  is promised, an important feature for stable  
269 ion-beam production.

270 Key to the operation of this configuration is a system that refreshes the target material at high-repetition  
271 rate in a reproducible manner. A number of schemes have been proposed for such studies, from high-  
272 pressure gases [Willingale et al. (2009); Bin et al. (2015); Chen et al. (2017)], cryogenic hydrogen ribbons  
273 [Margarone et al. (2016); Gauthier et al. (2017); Obst et al. (2017)], liquid sheets [Morrison et al. (2018)]  
274 and tape drives [Noaman-ul Haq et al. (2017)]. For the LhARA facility, a tape drive based on the system  
275 developed at Imperial College London is proposed. This system is capable of reliable operation at target  
276 thicknesses down to  $5 \mu\text{m}$ , using both aluminium and steel foils, and down to  $18 \mu\text{m}$  using plastic tapes.  
277 Such tape-drive targets allow operation at high charge (up to 100 pC at  $15 \pm 1$  MeV, i.e.  $> 10^9$  protons per  
278 shot) and of delivering high-quality proton and ion fluxes at repetition rates of up to 10 Hz or greater.

279 The careful control of the tension on the tape in a tape-drive target is critical for reproducible operation.  
280 The tape must be stretched to flatten the surface, without stretching it to its plastic response. Surface  
281 flatness is important for a number of reasons. Rippling of the front surface modifies the laser absorption  
282 dramatically; uncharacterised rippling can make shot-to-shot variations significant and unpredictable  
283 [Noaman-ul Haq et al. (2017)]. Similarly, rear surface perturbations can modify the sheath field, resulting  
284 in spatial non-uniformities of the proton beam or suppression of the achievable peak energies. Tape drives  
285 with torsion control and monitoring to maintain a high-quality tape surface have been designed and operated  
286 in experiments at Imperial College London. The development of these targets continues with a view to the  
287 production of new, thinner tapes for improved ion generation and the creation of ion species other than  
288 proton and carbon. This is an active area of R&D that will continue with the development of LhARA.

289 High repetition-rate ion-beam diagnostics will also need to be developed. Such diagnostics will need to  
290 measure both the energy spectrum and the spatial profile of the beams. Current methods are destructive and  
291 are often limited to low-repetition rate. Passive detectors have not been demonstrated in the conditions that  
292 will pertain at LhARA. Technologies being evaluated to address the issues raised by ion-source diagnostics  
293 for LhARA are discussed in section 3.5.

294

### 295 **3.2 Proton and ion capture**

296 The use of an electron cloud as a focusing element for charged-particle beams was first proposed by  
297 Gabor in 1947 [Gabor (1947)]. Gabor noted that a cloud of electrons uniformly distributed about the axis  
298 of a cylindrical vessel would produce an ideal focusing force on a beam of positively charged particles. The  
299 focal length of such a lens scales with the energy of the incoming particle beam allowing such lenses to  
300 provide strong focussing of high-energy beams. Confinement conditions in the radial and axial directions

301 can be determined [Pozimski and Aslaninejad (2013)]. In the radial direction, where there is magnetic  
 302 confinement and Brillouin flow, the number density of electrons,  $n_e$ , that can be contained is given by:

$$n_e = \frac{\epsilon_0 B^2}{2m_e}; \quad (1)$$

303 where  $B$  is the magnetic field,  $m_e$  the mass of the electron, and  $\epsilon_0$  the permittivity of free space. In the  
 304 longitudinal direction there is electrostatic confinement for which  $n_e$  is given by:

$$n_e = \frac{4\epsilon_0 V_A}{eR^2}; \quad (2)$$

305 where  $e$  the magnitude of the charge on the electron and  $R$  is the radius of the cylindrical anode which  
 306 is held at the positive potential  $V_A$ . For the electron densities of interest for LhARA the required anode  
 307 voltage is of the order of 50 kV.

308 In the thin lens approximation, the focal length,  $f$ , of a Gabor lens can be expressed in terms of the  
 309 magnetic field and the particle velocity,  $v_p$  [Reiser (1989)]:

$$\frac{1}{f} = \frac{e^2 B^2}{4m_e m_p v_p^2} l; \quad (3)$$

310 where  $m_p$  is the mass of the particles in the beam. The focal length of the Gabor lens is therefore  
 311 proportional to the kinetic energy or, equivalently, the square of the momentum, of the incoming beam. By  
 312 comparison, the focal length for a solenoid is proportional to the square of the momentum and that of a  
 313 quadrupole is proportional to momentum. At the particle energies relevant to LhARA the Gabor lens, or  
 314 the solenoid, is therefore preferred.

315 An expression for the focal length as a function of electron number density can be derived by substituting  
 316 equation (1) into equation (3) to give:

$$\frac{1}{f} = \frac{e^2 n_e}{4\epsilon_0 U} l; \quad (4)$$

317 where  $U = \frac{1}{2} m_p v_p^2$  is the kinetic energy of the particle beam. The focal length of the Gabor lens is inversely  
 318 proportional to the number density of electrons trapped in the cloud. The focal lengths desired to capture  
 319 the proton and ion beams at LhARA have been chosen such that the required electron number densities are  
 320 conservative and lie within the range covered in published experiments.

321 For a given focal length, the magnetic field required in the Gabor lens is reduced compared to that of a  
 322 solenoid that would give equivalent focusing. In the non-relativistic approximation the relationship between  
 323 the magnetic field in the Gabor lens,  $B_{GPL}$ , and the equivalent solenoid,  $B_{sol}$ , is given by [Pozimski and  
 324 Aslaninejad (2013)]:

$$B_{GPL} = B_{sol} \sqrt{Z \frac{m_e}{m_{ion}}}; \quad (5)$$

325 where  $m_{ion}$  is the mass of the ions being focused, and  $Z$  is the charge state of the ions. In the case of a  
 326 proton beam the reduction factor is 43. Thus, for example, where a 2 T superconducting solenoid would be  
 327 required, the magnetic field required for a Gabor lens would only be 47 mT. This means the cost of the  
 328 solenoid for a Gabor lens can be significantly lower than the cost for a solenoid of equivalent focusing  
 329 strength.

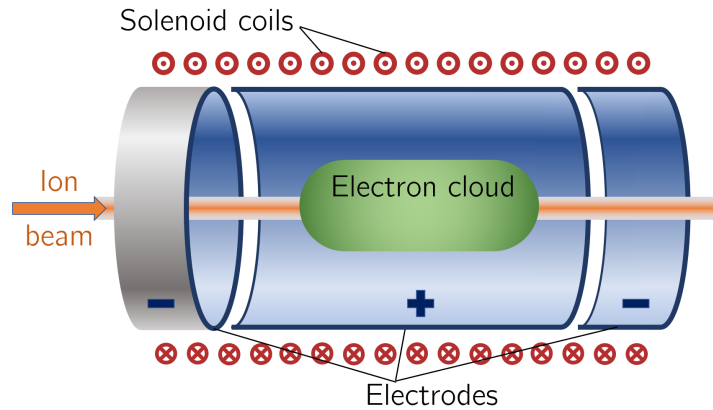


**Figure 2.** Schematic diagram of a Penning-Malmberg trap of the type proposed for use in the Gabor lenses to be used in LhARA. The solenoid coils, and the direction of current flow, are indicated by the red circles. The confining electrostatic potential is provided using a central cylindrical anode and two cylindrical negative end electrodes. The ion beam enters on-axis from the left and the electron cloud is indicated by the green shaded area.

330 The plasma-confinement system described above is commonly known as a ‘Penning trap’ and has found  
 331 wide application in many fields [Thompson (2015)]. Variations on the Penning trap where axial apertures  
 332 in the cathodes are introduced, such as the Penning-Malmberg trap [deGrassie and Malmberg (1980);  
 333 Malmberg et al. (1988)] are attractive for beam-based applications due to the excellent access provided to  
 334 the plasma column, see figure 2.

335 Instability of the electron cloud is a concern in the experimental operation of Gabor lens; azimuthal beam  
 336 disruption due to the diocotron instability has been observed and described theoretically [Meusel et al.  
 337 (2013)]. Theory indicates that the diocotron instability is most problematic under well-defined geometric  
 338 conditions. The reliable operation of a Gabor lens in a regime free from this instability has yet to be  
 339 demonstrated. Gabor lenses promise very strong focusing, simple construction, and low magnetic field,  
 340 all attractive features for LhARA. However, these attractive features come at the cost of relatively high  
 341 voltage operation ( $\gtrsim 50$  kV) and possible vulnerability to instability.

342 With reliable operation of Gabor lenses as yet unproven, we plan a two-part experimental and theoretical  
 343 programme of research to prove Gabor-lens suitability. Initial work will include: theoretical investigation  
 344 of lens stability in a full 3D particle-in-cell code such as VSIM [VSI (2020)]; and the development of  
 345 electron-density diagnostics based on interferometric measurement of the refractive-index change. These  
 346 activities will be applied to a time-invariant electron cloud. A test Gabor lens will be constructed to allow  
 347 validation of both the simulation results and a new diagnostic using an alpha emitter as a proxy for the  
 348 LhARA beam. In addition, the initial investigation will include the design of an electron beam to fill the  
 349 lens. This last objective will enable the second part of the experimental project; the operation of the Gabor  
 350 lens in short pulses. It is attractive to match the timing of the establishment of the electron cloud within the  
 351 Gabor lens to that of the beam and thereby limit instability growth. The research project is time limited  
 352 such that, should it not prove possible to produce a suitable Gabor lens, there will remain time sufficient to  
 353 procure conventional solenoids in their place.

354

### 3.3 Beam transport and delivery to the low-energy *in vitro* end station

Beam-transport from the laser-driven ion source and delivery to the low-energy *in vitro* end station is required to deliver a uniform dose distribution at the cell layer. Beam losses must be minimised for radiation safety and to maximise the dose that can be delivered in a single shot. The transport line has been designed to minimise regions in which the beam is brought to a focus to reduce the impact of space-charge forces on the beam phase-space. An optical solution was initially developed using Beamoptics [Autin et al. (1998)] and MADX [Grote and Schmidt (2003)]. Accurate estimation of the performance of the beam line requires the inclusion of space-charge forces and particle-matter interactions. Therefore, performance estimation was performed using Monte Carlo particle-tracking from the ion source to the end station. BDSIM [Nevay et al. (2020)], which is based on the Geant4 toolkit was used for the simulation of energy deposition arising from beam interactions with the material in the accelerator and the end station. GPT [De Loos and Van der Geer (1996)] was used for evaluating the full 3D impact of space-charge.

An idealised Gaussian beam was generated with a spot size of  $4\ \mu\text{m}$  FWHM, an angular divergence of 50 mrad, 35 fs FWHM bunch length, and an energy spread of  $1 \times 10^{-6}$  MeV. The maximum estimated bunch charge is  $1 \times 10^9$  protons. The presence of a substantial electron flux produced from the laser target compensates the high proton charge density in the vicinity of the ion-production point. Therefore, the first 5 cm of beam propagation was simulated without space-charge. Beyond this, the proton beam will have separated from the lower energy electrons sufficiently for space-charge to become a prominent effect and cause an emittance growth. Therefore, a further 5 cm drift was simulated including space-charge forces. At a distance of 10 cm from the ion source the beam is at the exit of the laser-target vessel. The kinematic distributions of ions in the beam were stored at this point and passed to the relevant BDSIM and GPT simulations of the downstream beam line.

The beam line, shown schematically in figure 3, is composed of five sections: beam capture; matching and energy selection; beam shaping; vertical arc matching; and an abort line. The capture section uses two Gabor lenses to minimise the transverse momentum of particles in the beam. Beyond the capture section, an RF cavity permits control of the bunch length and manipulation of the longitudinal phase-space. A third Gabor lens then focuses the bunch to a small spot size after which a second RF cavity is located to provide further longitudinal phase-space manipulation. Two further Gabor lenses bring the beam parallel once more in preparation for the vertical  $90^\circ$  arc. All Gabor lenses have an inner radius of 3.65 cm and an effective length of 0.857 m. All lenses operate below the maximum cathode voltage of 65 kV.

A parallel beam emerges from the final Gabor lens, providing significant flexibility for the inclusion of beam shaping and extraction systems. Beam uniformity will be achieved using octupole magnets to provide third-order focusing to perturb the first-order focusing from the Gabor lenses. Such schemes have been demonstrated in a number of facilities [Tsoupas et al. (1991); Urakabe et al. (1999); Amin et al. (2018)]. A suitable position for the first octupole was identified to be after the final Gabor lens where the beam is large; its effect on the beam is expected to be significant. Octupoles were only modelled in BDSIM as GPT does not have a standard component with an octupolar field. The typical rectangular transverse distribution resulting from octupolar focusing requires collimation to match the circular aperture through which the beam enters the end station. A collimator is therefore positioned at the start of the vertical arc. Further simulations are required to determine the optimum position of the second octupole and to evaluate the performance of the octupoles. The switching dipole which directs the beam to the injection line of the FFA in Stage 2 will be located between the second octupole and the collimator, requiring the octupole to be ramped down for Stage 2 operation.

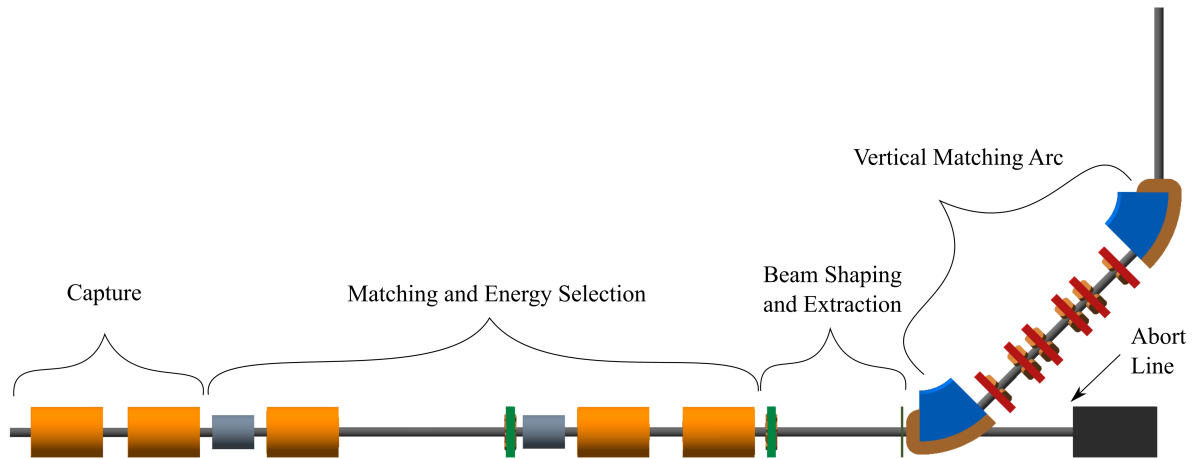


**Figure 3.** Beam transport for Stage 1 of LhARA visualised in BDSIM, showing five machine sections. The capture section is composed of two Gabor lenses (orange cylinders). The matching and energy selection section includes three Gabor lenses, two RF cavities (grey cylinders) and an octupole magnet (green disc). The beam shaping and extraction section includes a second octupole and a collimator (black vertical bar). The vertical matching arc directs the beam into the low-energy *in vitro* end station and is composed of two 45° dipoles and six quadrupoles. The total length of this beam line is 17.3 m.

398 The vertical arc uses transparent optics in an achromat matching section to ensure that the first-order  
 399 transfer map through the arc is equivalent to the identity transformation and that any dispersive effects are  
 400 cancelled. A 2 m drift tube is added after the arc to penetrate the concrete shielding of the end station floor  
 401 and to bring the beam to bench height. The abort line consists of a drift followed by a beam dump and  
 402 requires the first vertical dipole to ramp down, preventing charged-particle transportation to the end station.

403 The underlying physics of plasma-lens operation cannot be simulated in BDSIM or GPT, however it  
 404 can be approximated using solenoid magnets of equivalent strength. RF cavity fields were not simulated.  
 405 10 000 particles were simulated corresponding to the estimated maximum bunch charge of  $1 \times 10^9$  protons.  
 406 Figure 4 shows excellent agreement between horizontal and vertical transverse beam sizes in BDSIM  
 407 and MADX, verifying the beam line's performance in the absence of space-charge effects. Reasonable  
 408 agreement between BDSIM and GPT is also seen when space-charge forces are included in GPT. Emittance  
 409 growth is observed prior to the first solenoid, affecting the optical parameters throughout the machine.  
 410 However, the resulting beam dimensions at the cell layer of 1.38 cm horizontally and 1.47 cm vertically  
 411 are not significantly different from the ideal beam in BDSIM. Further adjustments of the Gabor lenses  
 412 and arc-quadrupole strengths may compensate for this. The transmission efficiency of the beam line is  
 413 approximately 100%.

414 The small bunch dimensions in both transverse planes at the focus after the third Gabor lens, where  
 415 the energy selection collimator will be placed, remains a concern if the effect of space-charge has been  
 416 underestimated. Similar bunch dimensions are achieved in the vertical arc, however, quadrupolar focusing  
 417 is confined to a single plane mitigating further emittance growth. Further tuning of the Gabor lens voltages  
 418 in the capture section may compensate space-charge effects, reducing the non-zero transverse momentum  
 419 seen entering the vertical arc.

420 To investigate beam uniformity, BDSIM simulations with and without octupoles and collimation for beam  
 421 shaping were conducted. Both octupoles were arbitrarily set to a strength of  $K3 = 6000$  with a magnetic

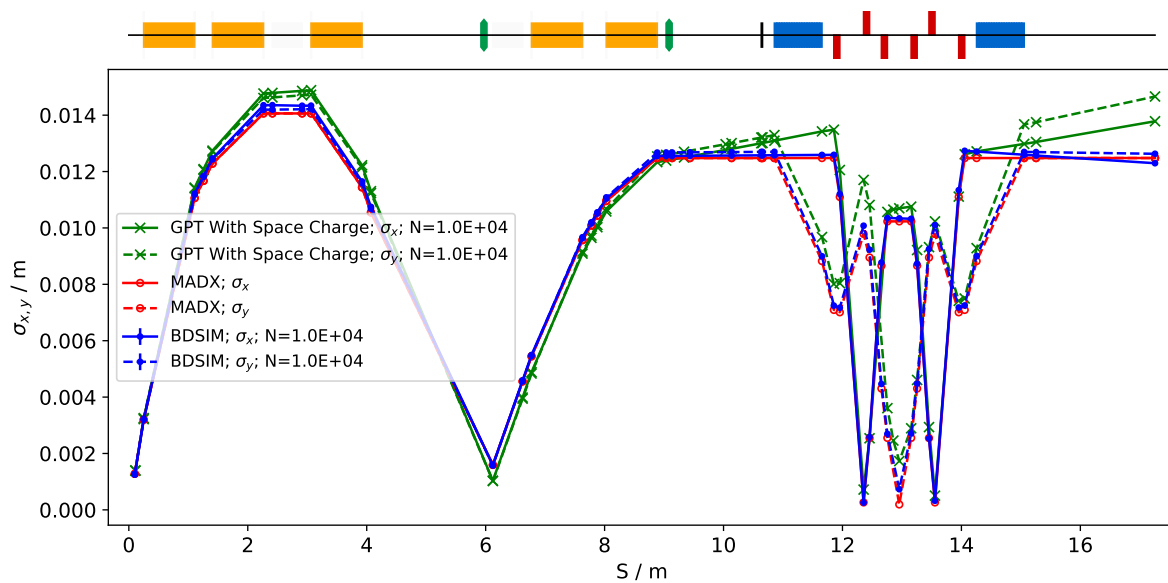


**Figure 4.** Horizontal (solid lines) and vertical (dashed lines) beam sizes through the *in vitro* beam transport, simulated with space-charge in GPT (green), and without space-charge in MADX (red) and BDSIM (blue).

422 length of 0.1 m and pole-tip radius of 5 cm, which, for a 15 MeV beam corresponds to pole-tip field of  
 423 0.42 T. A 2 cm thick iron collimator with a 40 mm diameter aperture was positioned 1.5 m downstream  
 424 of the octupole. Figure 5 shows the beam phase-space and particle distributions at the end station for the  
 425 transverse and longitudinal axes with and without beam shaping. Without octupoles the spatial profile  
 426 is Gaussian as expected, however, beam uniformity is improved with octupoles and collimation. The  
 427 total beam width is 3.58 cm horizontally and 3.46 cm vertically which is sufficient to irradiate one well  
 428 in a six-well cell-culture plate. Further optimisation is required to improve uniformity whilst optimising  
 429 beam-line transmission, which is approximately 70% for the results presented in figure 5. An aberration  
 430 can be seen in both transverse planes with and without beam shaping; this effect originates upstream of  
 431 the octupoles in the solenoids, and persists through to the end station. These aberrations are a concern,  
 432 however, future simulation efforts will replace the solenoids with a full electromagnetic simulation of the  
 433 Gabor lens. This change is likely to change the aberrations. The non-Gaussian energy distribution without  
 434 beam shaping is a result of space-charge forces at the ion source; the distribution persists to the end station  
 435 as no components which affect the longitudinal phase space were simulated. The Gaussian distribution  
 436 seen with beam shaping is due to collimation.

437 The proposed design is capable of delivering beams of the desired size to the *in vitro* end station. Space-  
 438 charge effects impact the beam-transport performance but it is believed that this can be mitigated with  
 439 minor adjustments to the Gabor lenses in the capture section. Initial studies indicate that a uniform beam  
 440 can be delivered with further optimisation of the octupoles and collimator.

441

### 442 3.3.1 Alternative Design

443 To mitigate potential emittance growth from space-charge forces, an alternative beam line design was  
 444 developed in which the final two Gabor lenses in the matching and energy selection section are replaced by  
 445 four quadrupoles, limiting any bunch focusing to one plane at a time. The resulting machine is reduced  
 446 in length to 15.439 m. Without space-charge effects, a beam sigma of 2.5 mm at the end station can be

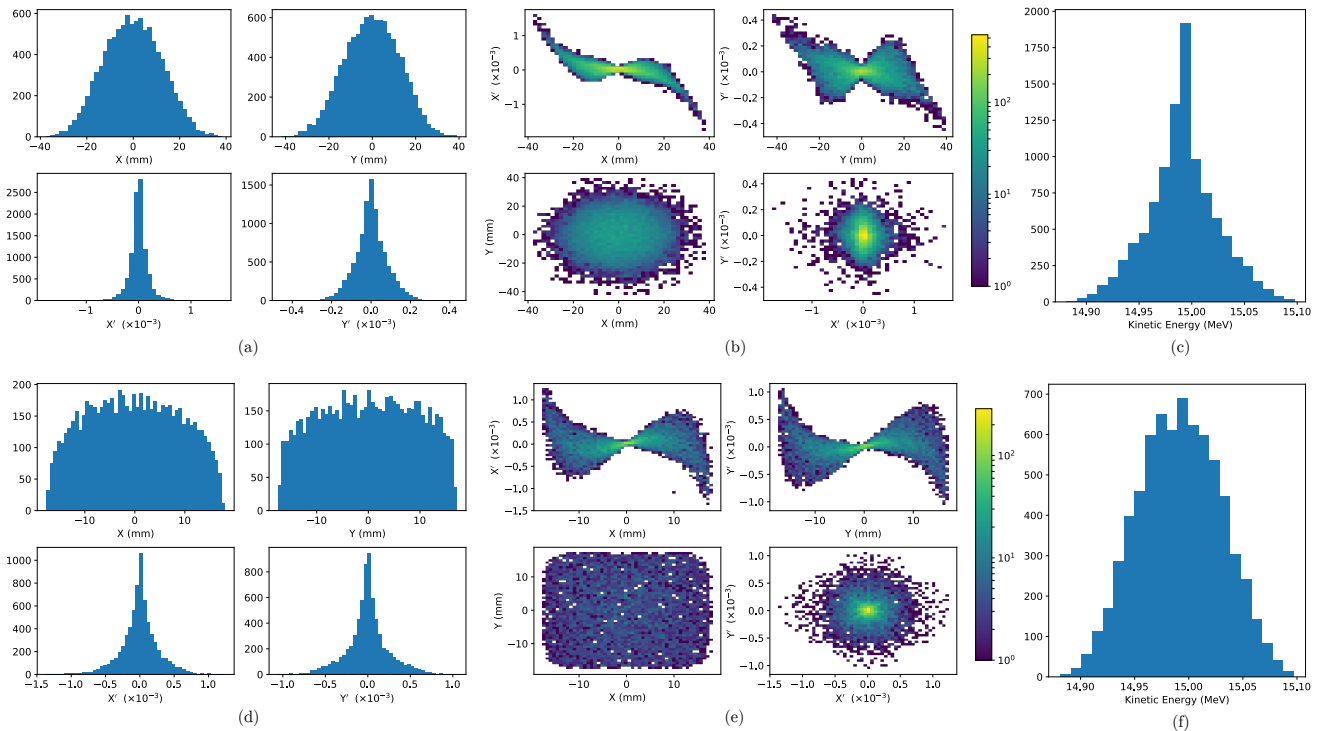


**Figure 5.** Beam phase space distributions at the end-station in the transverse plane,  $(X, Y)$ ;  $X'$  and  $Y'$  give the slope relative to the  $Z$  axis. The transverse phase space is shown in figures a and b for simulations without octupolar focusing and collimation, with the kinetic energy distribution shown in c. The same phase space distributions simulated with the effect of octupoles and collimation are in figures d, e, and f.

447 achieved. With space-charge, emittance growth prior to the first solenoid is once again observed leading  
 448 to an increased beam size at the entrance of the first quadrupole, resulting in a spatially asymmetric and  
 449 divergent beam at the end station. It is believed that the space-charge effects can be compensated by  
 450 applying the same Gabor-lens optimisation as in the baseline design and adjusting the quadrupole settings  
 451 to deliver beam parameters similar to those without achieved in the absence of space charge. The alternative  
 452 design provides a solution that is more resilient to space-charge effects than the baseline, however, only the  
 453 lower bound on the desired beam size has been achieved so far. Further optimisation is required not only to  
 454 optimise optical performance but also to optimise octupole settings and to determine whether a beam with  
 455 the desired uniformity can be delivered to the end station.

### 456 3.4 Post-acceleration and beam delivery to the *in vitro* and *in vivo* end stations

458 A fixed-field alternating-gradient accelerator (FFA), based on the spiral scaling principle [Krest et al.  
 459 (1956); Symon et al. (1956); Fourier et al. (2008); Tanigaki et al. (2006)], will be used to accelerate the  
 460 beam in LhARA Stage 2 to obtain energies greater than the 15 MeV protons and 4 MeV/u carbon ( $C^{6+}$ )  
 461 ions delivered by the laser-driven source. FFAs have many advantages for both medical and radiobiological  
 462 applications such as: the capability to deliver high and variable dose; rapid cycling with repetition rates  
 463 ranging from 10 Hz to 100 Hz or beyond; and the ability to deliver various beam energies without the use  
 464 of energy degraders. An FFA is relatively compact due to the use of combined function magnets, which  
 465 lowers the overall cost compared to conventional accelerators capable of delivering beams at a variety of  
 466 energies such as synchrotrons. Extraction can be both simple and efficient and it is possible for multiple

467 extraction ports to be provided. Furthermore, FFAs can accelerate multiple ion species, which is very  
468 important for radiobiological experiments and typically very difficult to achieve with cyclotrons.

469 A typical FFA is able to increase the beam momentum by a factor of three, though a greater factor may  
470 be achieved. For LhARA, this translates to a maximum proton-beam energy of 127 MeV from an injected  
471 beam of 15 MeV. For carbon ions ( $C^{6+}$ ) with the same rigidity, a maximum energy of approximately  
472 33.4 MeV/u can be produced.

473 The energy at injection into the FFA determines the beam energy at extraction. The injection energy will  
474 be changed by varying the focusing strengths in the Stage 1 beam line from the capture section through to  
475 the extraction line and the FFA ring. This will allow the appropriate energy slice from the broad energy  
476 spectrum produced at the laser-driven source to be captured and transported to the FFA. The FFA will then  
477 accelerate the beam, acting as a three-fold momentum multiplier. This scheme simplifies the injection and  
478 extraction systems since their geometry and location can be kept constant.

479 A second, ‘high-energy’, *in vitro* end station will be served by proton beams with a kinetic energy in the  
480 range 15–127 MeV and carbon-ion beams with energies up to 33.4 MeV/u. The extraction line from the  
481 FFA leads to a  $90^\circ$  vertical arc to send the beam to the high-energy *in vitro* end station. If the first dipole  
482 of the arc is not energised, beam will be sent to the *in vivo* end station. The extraction line of the FFA  
483 includes a switching dipole that will send the beam to the high-energy-beam dump if it is not energised.  
484 The detailed design of the high-energy abort line, taking into account the requirement that stray radiation  
485 does not enter the end stations, will be performed as part of the LhARA R&D programme.

486

#### 487 3.4.1 Injection line

488 The settings of the Stage 1 beam line need to be adjusted to reduce the Twiss  $\beta$  function propagating  
489 through the injection line to allow beam to be injected into the FFA ring. The optical parameters in the  
490 Stage 1 beam line after adjustment are shown in figure 6. The beam is diverted by a switching dipole into  
491 the injection line which transports the beam to the injection septum magnet. The injection line matches  
492 the Twiss  $\beta$  functions in both transverse planes and the dispersion of the beam to the values dictated by  
493 the periodic conditions in the FFA cell (figure 6). The presence of dispersion in the injection line allows a  
494 collimator to be installed for momentum selection before injection. The beam is injected from the inside of  
495 the ring, which requires the injection line to cross one of the straight sections between the FFA magnets,  
496 see figure 7.

497

#### 498 3.4.2 FFA ring

499 The magnetic field,  $B_y$ , in the median plane of a scaling spiral FFA is given by [Krest et al. (1956); Symon  
500 et al. (1956); Fourier et al. (2008)]:

$$B_y = B_0 \left[ \frac{R}{R_0} \right]^k F \left( \theta - \ln \left[ \frac{R}{R_0} \right] \tan \zeta \right); \quad (6)$$

501 where  $B_0$  is the magnetic field at radius  $R_0$ ,  $k$  is the field index,  $\zeta$  corresponds to the spiral angle and  $F$   
502 is the ‘flutter function’. This field law defines a zero-chromaticity condition, which means the working  
503 point of the machine is independent of energy up to field errors and alignment imperfections. This avoids  
504 crossing any resonances, which would reduce the beam quality and may lead to beam loss.

505 Table 2 gives the main design parameters of the FFA ring. The ring consists of ten symmetric cells each  
506 containing a single combined-function spiral magnet. The choice of the number of cells is a compromise

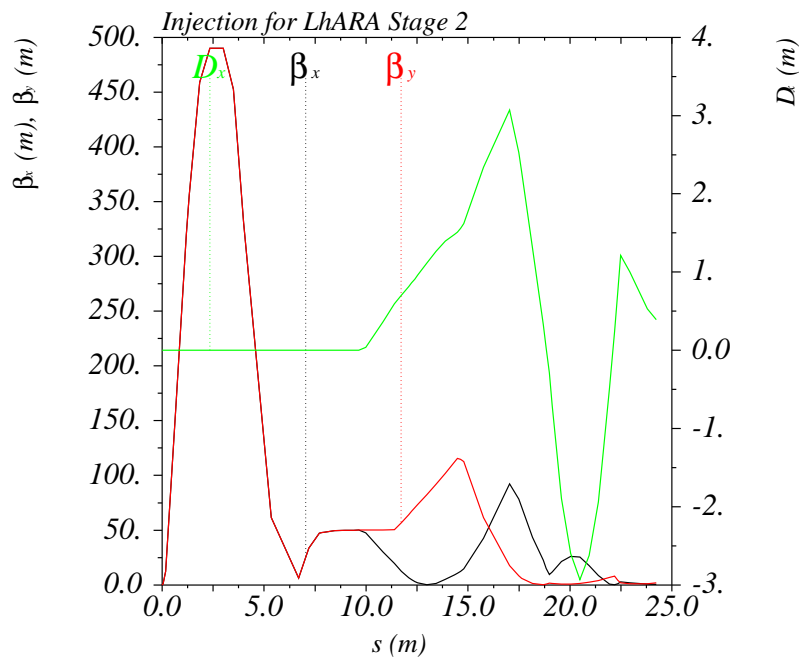


**Figure 6.** Twiss  $\beta_x$  and  $\beta_y$  functions and dispersion in the beam line consisting of the modified Stage 1 lattice and the transfer line allowing injection of the beam into the FFA ring.  $S$  goes from the laser target to the exit of the injection septum.

507 between the size of the orbit excursion, which dictates the radial extent of the magnet, and the length of the  
 508 straight sections required to accommodate the injection and extraction systems.

509 The betatron functions and dispersion in one lattice cell at injection are shown in figure 8a. The tune  
 510 diagram, showing the position of the working point of the machine in relation to the main resonance  
 511 lines, is shown in figure 8b. Tracking studies were performed using a step-wise tracking code in which the  
 512 magnetic field is integrated using a Runge-Kutta algorithm [Lagrange et al. (2018)]. The magnetic field in  
 513 the median plane was obtained using the ideal scaling law (equation 6) and using using Enge functions to  
 514 give the fringe fields. The field out of the median plane was obtained using Maxwell's equations and a  
 515 6<sup>th</sup>-order Taylor expansion of the field. The dynamic acceptance for 100 turns, shown for the horizontal  
 516 and vertical planes in figures 8c and 8d respectively, are significantly larger than the beam emittance. This  
 517 statement holds even when the most pessimistic scenario, in which the emittance is assumed to be ten times  
 518 larger than nominal, is used. These results confirm that a good machine working point has been chosen.

519 A full aperture, fast injection of the beam will be performed using a magnetic septum, installed on the  
 520 inside of the ring, followed by a kicker magnet situated in a consecutive lattice cell, as shown in figure 7.  
 521 The specifications of the injection system are dictated by the parameters of the beam at injection, which are  
 522 summarised for the nominal proton beam in table 3. The beam at injection has a relatively small emittance  
 523 and short bunch length, which limits the intensity accepted by the ring due to the space-charge effect. An  
 524 intensity of approximately  $10^9$  protons will be accepted by the ring assuming the nominal beam parameters.  
 525 Space-charge effects will be severe immediately after injection, but will quickly be reduced due to the  
 526 debunching of the beam. Fast extraction of the beam over the full aperture will be performed using a kicker  
 527 magnet followed by a magnetic septum installed in a consecutive lattice cell close to the extraction orbit.

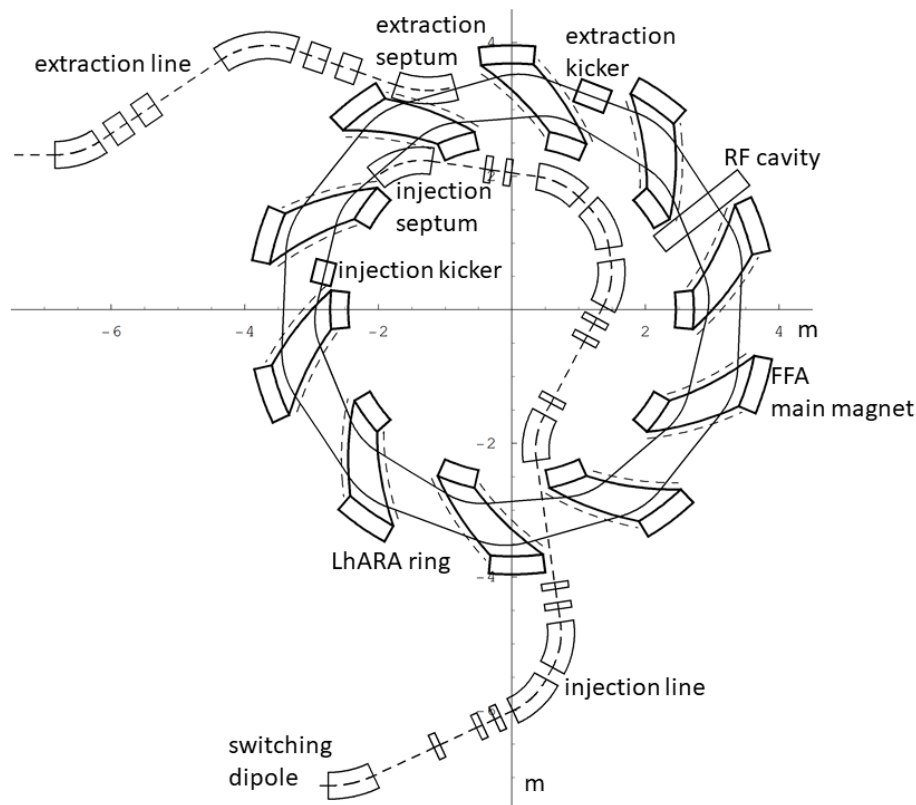


**Figure 7.** The layout of the injection line from the switching dipole to the injection septum together with the FFA ring, some of its subsystems and the first part of the extraction line.

**Table 3.** Summary of the main parameters for the proton beam at the injection to the FFA ring. These parameters correspond to the nominal (maximum) acceleration mode of operation.

Parameter	Unit	Value
Beam energy	MeV	15
Total relative energy spread	%	$\pm 2$
Nominal physical RMS emittance (both planes)	$\pi$ m rad	$4.1 \times 10^{-7}$
Incoherent space charge tune shift		-0.8
Bunching factor		0.023
Total bunch length	ns	8.1
Bunch intensity		$10^9$

528 Acceleration of the beam to 127 MeV will be done using an RF system operating at harmonic number  
 529  $h = 1$  with an RF frequency range from 2.89 MHz to 6.48 MHz. The RF voltage required for 10 Hz  
 530 operation is 0.5 kV. However, at such a low voltage the energy acceptance at injection will be limited to  
 531  $\pm 0.7\%$  so a voltage of 4 kV is required to increase the energy acceptance to  $\pm 2\%$ . This voltage can be  
 532 achieved with one cavity [Yonemura et al. (2008)], two cavities are assumed to provide greater operational  
 533 stability. Normal conducting spiral-scaling FFA magnets, similar to the ones needed for LhARA, have  
 534 been constructed successfully [Tanigaki et al. (2006); Planche et al. (2009)] using either distributed,  
 535 individually-powered coils on a flat pole piece or using a conventional gap-shaping technique. For the  
 536 LhARA FFA, we propose a variation of the coil-dominated design recently proposed at the Rutherford  
 537 Appleton Laboratory in R&D studies for the upgrade of the ISIS neutron and muon source. In this case, the

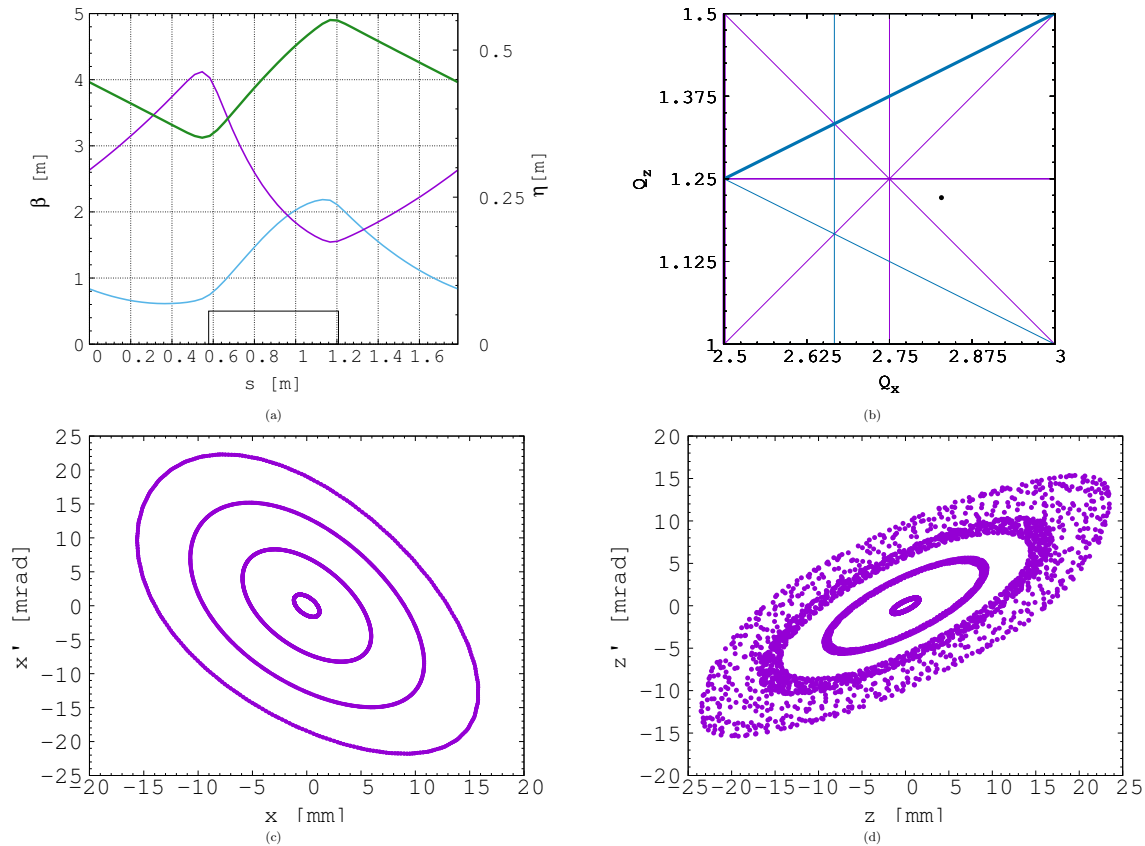


**Figure 8.** Beam optics and tracking in the FFA. Twiss  $\beta_h$  (blue),  $\beta_v$  (purple) functions and dispersion (green) in one lattice cell of the FFA ring (a). The working point of the FFA ring at (2.83, 1.22) on the tune diagram (b). The results of the horizontal (c) and vertical (d) dynamical acceptance study in the FFA ring, where a 1 mm offset is assumed in the vertical and horizontal planes respectively.

538 nominal scaling field is achieved using a distribution of single-powered windings on a flat pole piece. The  
 539 parameter  $k$  can then be tuned using up to three additional independently-powered windings. The extent  
 540 of the fringe field across the radius of the magnet must be carefully controlled using a ‘field clamp’ to  
 541 achieve zero-chromaticity. An active clamp, in which additional windings are placed around one end of the  
 542 magnet, may be used to control the flutter function and thereby vary independently the vertical tune of the  
 543 FFA ring. The FFA is required to deliver beams over a range of energy; each energy requiring a particular  
 544 setting for the ring magnets. Therefore, a laminated magnet design may be required to reduce the time  
 545 required to change the field. The magnet gap of 4.7 cm given in table 2 is estimated assuming a flat-pole  
 546 design for the magnet. The details of the design will be addressed in as part of the LhARA R&D programme.

### 547 548 3.4.3 Extraction Line

549 Substantial margins in the beam parameters were assumed in the design of the extraction line from the  
 550 FFA due to uncertainties in the beam distributions originating from: the Stage 1 beam transport; the  
 551 FFA injection line; and potential distortions introduced by the presence of space-charge effects during  
 552 acceleration in the ring. Therefore, the beam emittance was allowed, pessimistically, to be as large as a  
 553 factor of ten greater than in the nominal value, which was derived assuming that the normalised emittance  
 554 is conserved from the source, through the Stage 1 beam line, and in the FFA ring. In the nominal case,  
 555 the physical emittance of the beam is affected by adiabatic damping only. Substantial flexibility in the

**Table 4.** Beam emittance values and target  $\beta$  values for different beam sizes for 40 MeV and 127 MeV beams. The beam size is taken to be four times the sigma of the transverse beam distribution.

	40 MeV protons (Nominal)	127 MeV protons (Nominal)	127 MeV protons (Pessimistic)
RMS Emittance ( $\epsilon_x, \epsilon_y$ ) [ $\pi$ mm mrad]	0.137	0.137	1.37
$\beta$ [m] for a 1 mm spot size	0.46	0.46	0.039
$\beta$ [m] for a 10 mm spot size	46	46	4.5
$\beta$ [m] for a 30 mm spot size	410	410	40

556 optics of the extraction line is required, as the extraction line must accommodate a wide spectrum of beam  
557 conditions to serve the *in vitro* and *in vivo* end-stations.

558 Detailed studies were carried out for proton beams with kinetic energies of 40 MeV and 127 MeV. Table  
559 4 gives the Twiss  $\beta$  values for different beam sizes for the 40 MeV and 127 MeV proton-beam scenarios  
560 assuming a Gaussian beam distribution. The optics and geometric acceptance of the system is approximately  
561 the same for the 40 MeV and 127 MeV beams. This justified the working hypothesis that beam emittance is  
562 approximately the same for both beam energies. This assumption will be revised as soon as space-charge  
563 simulations for the entire system are available.

564 The first two dipoles and four quadrupoles of the extraction line bend the beam coming from the extraction  
565 septum of the FFA such that it is parallel to the low-energy beam line while ensuring that dispersion is  
566 closed. Closing the dispersion is critical as off-momentum particles will follow trajectories different to  
567 those followed by particles with the design momentum and therefore impact the size and shape of the beam  
568 downstream. The second part of the extraction line consists of four quadrupoles which transport the beam  
569 either to the first dipole of the vertical arc that serves the high-energy *in vitro* end station or to the *in vivo*  
570 end-station if this dipole is not energised. These quadrupoles provide the flexibility required to produce the  
571 different beam sizes for the *in vitro* end station as specified in table 4.

572

#### 573 3.4.4 High-energy *in vitro* beam line

574 The high-energy *in vitro* beam line transports the beam from the exit of the extraction line and delivers it to  
575 the high-energy *in vitro* end station. The 90° vertical bend is a scaled version of the low-energy vertical arc,  
576 following the same design principles, and also consists of two bending dipole magnets and six quadrupole  
577 magnets. To accommodate the higher beam energies, the lengths of the magnets were scaled in order to  
578 ensure that peak magnetic fields were below the saturation limits of normal conducting magnets. The  
579 bending dipole magnet lengths were increased to 1.2 m each and the quadrupole lengths were tripled to  
580 0.3 m each. The overall length of the arc then becomes 6 m, compared to 4.6 m for the low energy *in vitro*  
581 arc. This difference in arc length means the high-energy *in vitro* arc finishes about 0.9 m higher than the  
582 low-energy one. This difference can easily be accommodated by adjusting the final drift lengths.

583 The quadrupole strengths for the scaled high-energy *in vitro* arc were obtained using MAD-X and  
584 tracking simulations using BDSIM show good agreement, see figure 9. The input beam distribution used  
585 in BDSIM was assumed to be Gaussian with Twiss  $\beta = 46$ , which gives a beam size of about 10 mm.  
586 GPT simulations were performed which show small discrepancies due to space-charge effects. It may be  
587 possible to compensate for this by adjusting the strengths of the quadrupoles in the arc and the matching  
588 section in the extraction line.

589

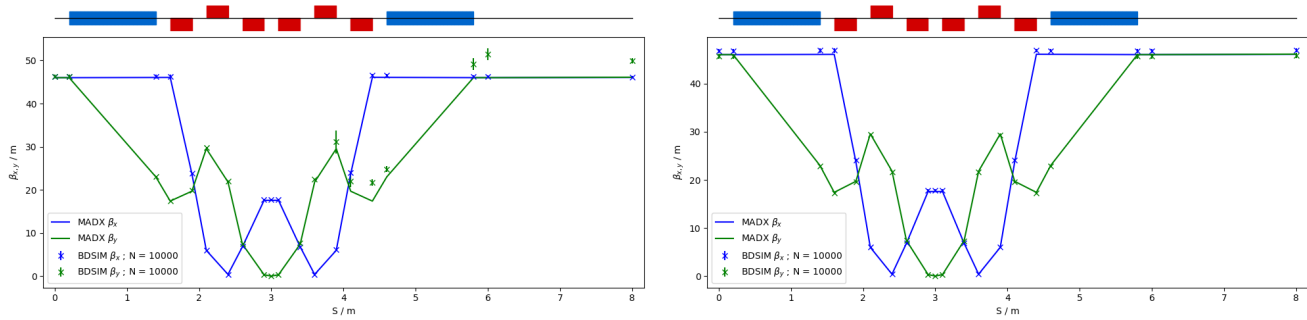


**Figure 9.** Comparison of MAD-X and BDSIM simulation of 40 MeV (left) and nominal 127 MeV (right) proton beam passing through the high energy *in vitro* arc simulated with  $10^4$  particles (in BDSIM).

### 590 3.4.5 *In vivo* beam line

591 To facilitate efficient small-animal handling, an end station dedicated to *in vivo* experiments has been  
 592 positioned adjacent to the principle road access to the facility. If the first dipole of the high-energy *in vitro*  
 593 arc is not energised, the beam is sent to the *in vivo* end station. From the end of the extraction line, 7.7 m of  
 594 drift is necessary to clear the first bending dipole of the *in vitro* arc, to provide space for the five RF cavities  
 595 needed for longitudinal phase-space manipulation and to allow space for diagnostic devices. Following this  
 596 drift is a further 6.6 m of beam line that includes four quadrupoles, each of length 0.4 m, which are used to  
 597 perform the final focusing adjustments of the beam delivered to the *in vivo* end station. A final 1.5 m drift  
 598 at the end is reserved for scanning magnets to be installed to perform spot scanning and to penetrate the  
 599 shielding of the *in vivo* end station. In total the *in vivo* beam line is 15.6 m in length.

600 The design is flexible in matching the various  $\beta_{x,y}$  values given in table 4, but is not able to match  
 601 the smallest target value of  $\beta_{x,y} = 0.039$  m for the pessimistic scenario, which is very challenging. To  
 602 verify that the optics design could provide the required beam sizes, simulations were performed with  
 603 BDSIM using an input Gaussian beam generated with the Twiss  $\beta$  values given in tables 4. Figure 10  
 604 shows the results of simulations for a 40 MeV proton beam and a nominal emittance 127 MeV proton  
 605 beam matched in order to obtain beam sizes of 1 mm, 10 mm and 30 mm. GPT was used to investigate the  
 606 effects of space-charge. These simulations show discrepancies compared to the BDSIM simulations. These  
 607 discrepancies can be compensated for by adjusting the strengths of the quadrupoles in the matching section  
 608 in the extraction line.

## 609 3.5 Instrumentation

611 Commercial off-the-shelf (COTS) instrumentation will be used for Stages 1 and 2 of LhARA wherever  
 612 possible. However, the characteristics of the beam (e.g. very high charge-per-bunch, low-to-moderate  
 613 energy) will require some custom solutions to be developed. The authors are developing two concepts,  
 614 termed SciWire and SmartPhantom, for the low- and high-energy *in vitro* end stations respectively. These  
 615 detectors can also be used for beam diagnostics. This new instrumentation may find application at other  
 616 facilities. Instrumentation for the detection of secondary particles arising from the interaction of the beam  
 617 with tissue is not discussed here but is an important area that will be studied in the future.

### 618 3.5.1 SciWire

620 For the Stage 1 beam, the maximum proton energy is 15 MeV. Shot-to-shot characterisation of the beam is  
 621 essential and requires the use of a very thin detector with a fast response. The SciWire [Kurup (2019)] is

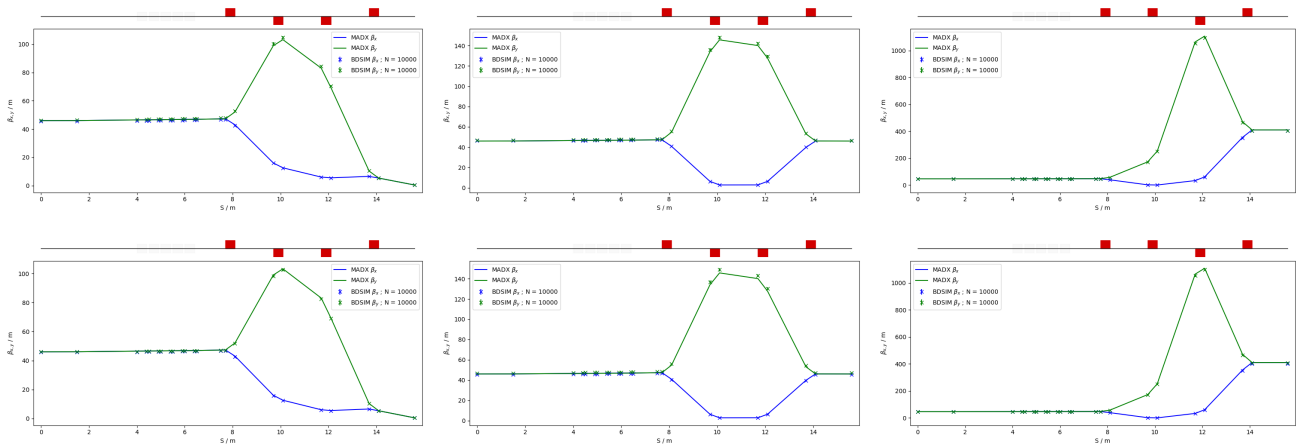


**Figure 10.** MAD-X and BDSIM simulations of the *in vivo* beam line for a 40 MeV proton beam (top row) and a nominal 127 MeV proton beam (bottom row) with quadrupoles matched to  $\beta_{x,y} = 0.46$  m (left),  $\beta_{x,y} = 46$  m (middle) and  $\beta_{x,y} = 410$  m (right) for  $10^4$  particles.

622 being developed to provide energy and intensity profile measurements for low-energy ion beams. A single  
 623 SciWire plane consists of two layers of  $250 \mu\text{m}$  square-section scintillating fibres, with the fibre directions  
 624 in the two layers orthogonal to each other. A series of back-to-back planes provides a homogeneous volume  
 625 of scintillator. If there are enough planes to stop the beam, the depth of penetration will allow the beam  
 626 energy to be inferred. This is obviously a destructive measurement so it is envisaged that this type of  
 627 measurement would only be used when experiments are not running. A single plane, however, can be used  
 628 for 2D beam-profile measurements at the same time that beam is delivered for experiments. Detection of  
 629 the light from SciWire fibres may be by CMOS camera, or using photodiodes. If the instrumentation is  
 630 sufficiently fast, the SciWire can be used to derive feedback signals for beam tuning.

### 631 3.5.2 SmartPhantom

633 To study in real time the dose profile of Stage 2 beams, the SmartPhantom [Barber (2018)] is being  
 634 developed. This is a water-filled phantom, which is instrumented with planes of scintillating fibres, by  
 635 which to infer the dose distribution with distance. The detection elements of the SmartPhantom are  $250 \mu\text{m}$   
 636 diameter, round scintillating fibres. Each fibre station consist of two planes of fibres, in which the fibre  
 637 directions are orthogonal. Five fibre stations are arranged in the phantom in front of the cell-culture flask.  
 638 The fibres may be coupled to photodiodes, or a CMOS camera. Simulations in GEANT4 are being used to  
 639 develop analysis techniques by which to predict the position of the Bragg peak shot-by-shot. The beam  
 640 profile and dose delivered can then be calculated in real time. The key emphasis is to be able to derive these  
 641 parameters from shot-by-shot data, and not purely from simulations.

### 642 3.5.3 Beam line Instrumentation

644 The instrumentation requirement begins with the Ti:Sapphire laser. The laser focal spot will be characterised  
 645 using a camera-based system and high-speed wavefront measurements [Wang (2014)] from COTS vendors.

646 For the Stage 1 beam line, beam position monitors (BPMs) will be needed for beam steering. Because  
 647 of the low beam energy, non-intercepting BPMs using capacitive pickup buttons will be used. Custom  
 648 pickups will be needed to match the beam pipe geometry but COTS electronics are available. The beam  
 649 current will be monitored near the end of each beam line, using integrating current toroids (ICT), backed

650 up with the option of insertable multi-layer Faraday cups (MLFC) to give absolute beam current and energy  
651 measurements. Beam profiles could be measured by SEM grids on both Stage 1 and Stage 2 beam lines.  
652 For Stage 1, these monitors will be mounted on pneumatic actuators to avoid scattering. Each end station  
653 could be equipped with insertable “pepper-pot” emittance monitors and a transverse deflection cavity with  
654 fluorescent screen could be provided for bunch shape measurements.

655 The BPMs on the FFA will require pickup designs suitable for the unusual, wide and shallow, vacuum  
656 vessel. The FFA at the KURNS facility in Kyoto is of a similar layout [Uesugi (2018)] and uses a kicker  
657 and capacitive pickup to perform tune measurements in each transverse direction. A minimum of one BPM  
658 every second cell will be used in the FFA so that the beam orbit can be measured. BPMs will also be  
659 required close to the injection and extraction septa. The BPM system may be able to use COTS electronics,  
660 but the pickups will be based on the KURNS design of multiple electrodes arranged across the vacuum  
661 vessel width.

662 The data acquisition system needs to be able to store calibration data and apply corrections in real time. It  
663 is necessary to be able to find the beam centre from a profile, even when the profile may be non-Gaussian  
664 and possibly asymmetric. Field programmable gate arrays (FPGAs) can be used to perform fast fitting and  
665 pattern recognition of beam profiles. The instrumentation will be integrated with the accelerator control  
666 system to be able to provide fast feedback and adjustment of the beam parameters in real time.

667

### 668 **3.6 Biological end stations**

669 In order to deliver a successful radiobiological research programme, high-end and fully equipped *in vitro*  
670 and *in vivo* end-stations will be housed within the LhARA facility. The two *in vitro* end-stations (high  
671 and low energy) will contain vertically-delivered beam lines which will be used for the irradiation of 2D  
672 monolayer and 3D-cell systems (spheroids and patient-derived organoids) in culture. The beam line within  
673 the end-stations will be housed in sealed units that will be directly sourced with appropriate gases (carbon  
674 dioxide and nitrogen), allowing for the cells within culture plates to be incubated for a short time in stable  
675 conditions prior to and during irradiation. This will also enable the chamber to act, where necessary, as a  
676 hypoxia unit (0.1%–5% oxygen concentration). Furthermore, these sealed units will contain robotics to  
677 enable simple movement of the numerous cell culture plates housed within to be placed into and taken  
678 away from the beam.

679 The *in vitro* end-stations will be located within a research laboratory equipped with up-to-date and  
680 state-of-the-art facilities. The laboratory will include all the vital equipment for bench-top science, sample  
681 processing and analysis (e.g. refrigerated centrifuges and light/fluorescent microscopes), along with the  
682 equipment required for contaminant-free cell culture (e.g. humidified CO<sub>2</sub> cell culture incubators, Class II  
683 biological safety cabinets), and for the storage of biological samples and specimens (e.g. –20°C and –80°C  
684 freezers and fridges). The laboratory will also house an X-ray irradiator (allowing direct RBE comparisons  
685 between conventional photon irradiation, and the proton and carbon ions delivered by the accelerator),  
686 hypoxia chamber (for long-term hypoxia studies), a robotic workstation (handling and processing of large  
687 sample numbers, assisting in high-throughput screening experiments), and an ultra-pure-water delivery  
688 system. These facilities will enable a myriad of biological end-points to be investigated in both normal-  
689 and tumour-cell models not only from routine clonogenic survival and growth assays, but will expand  
690 significantly on more complex end-points (e.g. inflammation, angiogenesis, senescence and autophagy)  
691 as these experiments are difficult to perform at current clinical research beams due to limited time and  
692 facilities.

693 The *in vivo* end-station will be served with high-energy proton and carbon ions capable of penetrating  
694 deeper into tissues allowing the irradiation of whole animals. The ability to perform *in vivo* pre-clinical  
695 studies is vital for the future effective translation of the research into human cancer patients where optimum  
696 treatment strategies and reduction of side-effects can be defined. The *in vivo* end-station will allow the  
697 irradiation of a number of small-animal models (e.g. xenograft mouse and rat models) which can further  
698 promote an examination of particular ions on the appropriate biological end-points (e.g. tumour growth  
699 and normal tissue responses). The end-station will contain a small-animal handling area which will allow  
700 for the anaesthetisation of animals prior to irradiation. To enable the irradiation of small target volumes  
701 with a high level of precision and accuracy, an image guidance system (e.g. computed tomography) will be  
702 available. The animals will subsequently be placed in temperature-controlled holder tubes enabling the  
703 correct positioning of the relevant irradiation area in front of the beam line. The beam size is sufficient to  
704 give flexibility in the different irradiation conditions, in particular through passive scattering, pencil-beam  
705 scanning, and micro-beam irradiation, to be investigated at both conventional and FLASH dose rates. It is  
706 envisaged that the animals will be taken off-site post-irradiation to a nearby animal-holding facility for a  
707 follow-up period where biological measurements will be conducted.

708

### 709 3.7 Infrastructure and integration

710 The LhARA facility will encompass two floors of roughly 42 m in length and 18 m wide. The ground floor  
711 will contain the laser, accelerator, and *in vivo* end station while the first floor will house the laboratory area  
712 and the two *in vitro* end stations. The entire facility will require radiation protection in the form of concrete  
713 shielding, which will delineate the facility into three principal areas: a radiation-controlled access area, a  
714 laser controlled access area, and a laboratory limited-access area.

715 It is envisaged that LhARA will be built at a national Laboratory or equivalent research institute which  
716 has an established safety-management system and culture in place. At STFC, a comprehensive set of Safety  
717 Codes has been developed to cover the hazards associated with working in such an environment. STFC  
718 Safety Codes applicable to LhARA include: risk management, construction, biological safety, working  
719 with lasers, working with time-varying electro-magnetic fields, management of ionising radiation, and  
720 electrical safety. In practice at STFC, these codes are backed-up by the knowledge, skills and experience  
721 of staff, and by appointed responsible persons such as Radiation Protection Advisors, Laser Responsible  
722 Officers, and Authorising Engineers. In addition, STFC operates many facilities that encompass the same  
723 hazards as LhARA, which, for lasers, include the Gemini Target Areas 2 and 3 [STFC (2019a)] as well as  
724 the new EPAC (Extreme Photonics Application Centre) [STFC (2019b)] and for accelerators include FETS  
725 (Front End Test Stand) [Letchford et al. (2015)], and the ISIS Neutron and Muon Source [STFC (2019c)].  
726 Safety systems and equipment will be required for LhARA, which will include Class II biological safety  
727 cabinets for contaminant-free cell culture for *in vitro* radiobiological experiments.

728 For a facility such as LhARA, radiation safety is a primary concern and all work will be completed  
729 under Regulation 8 of the Ionising Radiations Regulations 2017 (IRR17) [HSE (2018)], which requires a  
730 radiation risk assessment before commencing a new work activity involving ionising radiation.

731 The infrastructure and integration of the LhARA facility will require R&D in four key areas: risk analysis  
732 (project risks), risk assessments (safety risks), radiation simulations, and controls development. The risk  
733 analysis will cover all aspects of the facility, such as funding and resource availability, not just technical  
734 risks. A safety-risk assessment will be performed to describe and control all potential safety risks in the  
735 facility. The safety-risk assessment will, to a reasonable degree, identify all pieces of equipment that  
736 require safety mitigations and identify control measures that must be put in place. Coupled closely with the

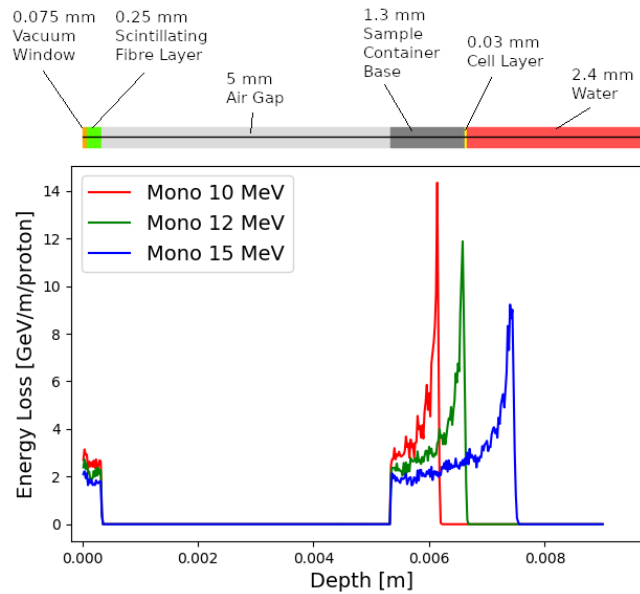


**Figure 11.** Energy loss as a function of depth in the low-energy *in vitro* end station for three monoenergetic proton energies: 10 MeV; 12 MeV; and 15 MeV. Each beam was simulated using  $10^4$  particles at the start of the simulated end station. The material through which the beam passes is indicated above the figure. The entrance window is plotted at a Depth value of 0 m. The beam deposits energy in the beam window and the layer of scintillating fibre before passing through the air and entering the sample container.

737 safety-risk assessment, radiation simulations will be developed to characterise the radiation hazards in and  
 738 around the LhARA facility. The last area to require R&D will be the control systems. It is expected that the  
 739 facility will use the Experimental Physics and Industrial Control System (EPICS), which can be further  
 740 developed at this stage.  
 741

#### 4 PERFORMANCE

742 The dose distributions delivered to the end stations were evaluated using BDSIM. Figure 11 shows the  
 743 energy lost by the beam as it enters the low-energy *in vitro* end station. The beam passes through the  
 744 vacuum window, a layer of scintillating fibre, and a 5 mm air gap. The beam then enters the cell-sample  
 745 container, assumed to be polystyrene, which supports a  $30\ \mu\text{m}$  thick layer of cells, modelled using the  
 746 Geant4 material “G4.SKIN\_ICRP” [NIST (2017)]. The transverse momentum of protons in the beam was  
 747 assumed to be Gaussian distributed, with a lateral spread small enough for the beam to be fully contained  
 748 within the required spot size of 3 cm. Figure 11 shows that a proton beam with 10 MeV kinetic energy  
 749 does not reach the cell. The Bragg peak of a 12 MeV proton beam is located close to the cell layer, while  
 750 a 15 MeV beam, the maximum energy specified for delivery to the low-energy *in vitro* end station, has  
 751 a Bragg peak located beyond the cell layer. LhARA’s ability to deliver various energies will allow the  
 752 investigation of radiobiological effects for irradiations using different parts of the Bragg peak, effectively  
 753 varying the LET across the sample. RF cavities are placed in both the stage 1 and the stage 2 beam lines to  
 754 allow the manipulation of the energy of the bunch as a function of time. This facility will allow the study  
 755 of the impact of a “spread-out Bragg peak” (SOBP).

756 The maximum dose that can be delivered was evaluated for a variety of beam energies. In order for the  
 757 dose to be reported in units of Gray it is necessary to define the volume within which the energy deposition

758 is to be integrated. Therefore, the dose was estimated from simulations by calculating the energy deposited  
759 in a volume of water corresponding in size to the sensitive volume of a PTW 23343 Markus ion chamber  
760 [PTW (2019/2020)] placed at the position of the Bragg peak in each case. This choice allows the doses and  
761 dose-rates reported below to be compared to other facilities which are in operation since the PTW 23343  
762 Markus ion chamber is widely at existing facilities. The cylindrical sensitive volume of the ion chamber  
763 has a radius of 2.65 mm and a depth of 2 mm, giving a volume of about  $4.4 \times 10^{-8} \text{ m}^3$ . The total energy  
764 deposited within the chamber was recorded and converted into dose in units of Gray.

765 For the low-energy *in vitro* end station the minimum spot size is specified to have a diameter of 10 mm,  
766 which is larger than the area of the chamber. A single shot of  $10^9$  protons at 12 MeV with the minimum  
767 design spot size deposits  $3.1 \times 10^{-4} \text{ J}$  in the chamber volume, corresponding to a dose of 7.1 Gy. For this  
768 simulation, the thickness of the sample container was reduced so that the Bragg peak could be positioned  
769 within the chamber volume. For the bunch length of 7.0 ns the maximum instantaneous dose rate is  
770  $1.0 \times 10^9 \text{ Gy/s}$  and the average dose rate is 71 Gy/s assuming a repetition rate of 10 Hz. A single shot of  
771  $10^9$  protons at 15 MeV deposits  $5.6 \times 10^{-4} \text{ J}$  in the chamber volume corresponding to a dose of 12.8 Gy.  
772 This gives an instantaneous dose rate of  $1.8 \times 10^9 \text{ Gy/s}$  and an average dose rate of 128 Gy/s assuming the  
773 same bunch length and repetition rate as for the 12 MeV case.

774 For the high-energy *in vitro* end station a different setup was used for high energy proton beams. A  
775 similar design to the low-energy end station was used but with the air gap increased from 5 mm to 5 cm and  
776 a water phantom was placed at the end of the air gap instead of a cell culture plate. The water phantom  
777 used in the simulation was based upon the PTC T41023 water phantom [PTW (2009)]. In addition, the  
778 smaller minimum design beam size of 1 mm was used. A single shot of  $10^9$  protons at 127 MeV deposits  
779  $6.9 \times 10^{-4} \text{ J}$  in the chamber at the pristine Bragg peak depth corresponding to a dose of 15.6 Gy, an  
780 instantaneous dose rate of  $3.8 \times 10^8 \text{ Gy/s}$  and an average dose rate of 156 Gy/s. The end-station design  
781 assumed for a 33.4 MeV/u carbon beam was the same as that used for the low-energy *in vitro* end station  
782 due to the limited range in water of the carbon beam. The intensity of the beam is a factor of 12 less than  
783 for protons in order to preserve the same strength of the space-charge effect at injection into the FFA with  
784 the same beam parameters, as the incoherent space charge tune shift is proportional to  $q^2/A$  and inversely  
785 proportional to  $\beta^2\gamma^3$ , where  $q$  corresponds to the particle charge,  $A$  its mass number and  $\beta$ ,  $\gamma$  its relativistic  
786 parameters. A single pulse of  $8.3 \times 10^7$  ions, deposits  $3.2 \times 10^{-3} \text{ J}$  at the depth of the pristine Bragg peak,  
787 leading to an instantaneous dose rate of  $9.7 \times 10^8 \text{ Gy/s}$  and a maximum average dose rate of 730 Gy/s.

788 The expected maximum dose rates are summarised in table 5. The instantaneous dose rates depend on  
789 the bunch length which differs depending on the energies. For the low-energy *in vitro* line a 7 ns bunch  
790 length is assumed here for all energies. While for the higher energies, a 127 MeV proton beam is delivered  
791 with a bunch length of 41.5 ns, and a bunch length of 75.2 ns for a 33.4 MeV/u carbon beam. The same  
792 repetition rate of 10 Hz was used for all energies. The minimum beam size at the start of the end station for  
793 the 12 MeV and 15 MeV proton-beam simulations was 1 cm. A 1 mm beam size was used for the 127 MeV  
794 proton beam and 33.4 MeV/u carbon-ion beam simulations.

795

## 5 CONCLUSIONS

796 The initial conceptual design of LhARA, the Laser-hybrid Accelerator for Radiobiological Applications,  
797 has been described and its performance evaluated in simulations that take into account the key features of  
798 the facility. LhARA combines a laser-driven source to create a large flux of protons or light ions which are  
799 captured and formed into a beam by strong-focusing plasma lenses thus evading the current space-charge

**Table 5.** Summary of expected maximum dose per pulse and dose rates that LhARA can deliver for minimum beam sizes. These estimates are based on Monte Carlo simulations using a bunch length of 7 ns for 12 MeV and 15 MeV proton beams, 41.5 ns for the 127 MeV proton beam and 75.2 ns for the 33.4 MeV/u carbon beam. The average dose rate is based on the 10 Hz repetition rate of the laser source.

	12 MeV Protons	15 MeV Protons	127 MeV Protons	33.4 MeV/u Carbon
Dose per pulse	7.1 Gy	12.8 Gy	15.6 Gy	73.0 Gy
Instantaneous dose rate	$1.0 \times 10^9$ Gy/s	$1.8 \times 10^9$ Gy/s	$3.8 \times 10^8$ Gy/s	$9.7 \times 10^8$ Gy/s
Average dose rate	71 Gy/s	128 Gy/s	156 Gy/s	730 Gy/s

800 limit on the instantaneous dose rate that can be delivered. Acceleration, performed using an fixed-field  
 801 alternating-gradient accelerator, preserves the unique flexibility in the time, spectral, and spatial structure  
 802 of the beam afforded by the laser-driven source. The ability to trigger the laser pulse that initiates the  
 803 production of protons or ions at LhARA will allow the time structure of the beam to be varied to interrupt  
 804 the chemical and biological pathways that determine the biological response to ionising radiation. In  
 805 addition, the almost parallel beam that LhARA will deliver can be varied to illuminate a circular area with  
 806 a maximum diameter of between 1 cm and 3 cm with an almost uniform dose or focused to a spot with  
 807 diameter of  $\sim 1$  mm. These features make LhARA the ideally flexible tool for the systematic study of the  
 808 radiobiology of proton and ion beams.

809 The laser-hybrid approach, therefore, will allow radiobiological studies and eventually radiotherapy to  
 810 be carried out in completely new regimes, delivering a variety of ion species in a broad range of time  
 811 structures and spatial configurations at instantaneous dose rates up to and potentially significantly beyond  
 812 the current ultra-high dose-rate “FLASH” regime. By demonstrating a triggerable system that incorporates  
 813 dose-deposition imaging in the fast feedback-and-control system, LhARA has the potential to lay the  
 814 foundations for “best in class” treatments to be made available to the many by reducing the footprint of  
 815 future particle-beam therapy systems.

816 LhARA has the potential to drive a change in clinical practice in the medium term by increasing the  
 817 wealth of radiobiological knowledge. This enhanced understanding in turn may be used to devise new  
 818 approaches to decrease radio-toxicity on normal tissue while maintaining, or even enhancing, the tumour-  
 819 control probability. The radiobiology programme in combination with the demonstration in operation of  
 820 the laser-hybrid technique means that the execution of the LhARA programme has the potential to drive a  
 821 step-change in the clinical practice of proton- and ion-beam therapy.

822

## ACKNOWLEDGEMENTS

823 The work described here was made possible by a grant from the Science and Technology Facilities Council  
 824 (ST/T002638/1, ST/P002021/1). Additional support was provided by the STFC Rutherford Appleton and  
 825 Daresbury Laboratories and members of the LhARA consortium. We gratefully acknowledge all sources  
 826 of support. A pre-publication review of the pre-CDR for LhARA was carried out by P. Bolton (LMU,  
 827 Munich), M. Lamont (CERN), Y. Prezado (Institut Curie), and F. Romano (INFN-LNS and the National  
 828 Physical Laboratory). We are grateful to the review panel for their support and detailed feedback on the  
 829 draft pre-CDR.

830

## REFERENCES

- 831 (2009). *User Manual Water Phantom T41023*. PTW-Freiburg Physikalisch-Technische Werkstätten Dr.  
832 Pychlau GmbH, d738.131.00/02 en edn.
- 833 (2019/2020). *Ionizing Radiation Detectors*. PTW-Freiburg Physikalisch-Technische Werkstätten Dr.  
834 Pychlau GmbH
- 835 [Dataset] (2020). Vsim for plasma. <https://www.txcorp.com/vsim>
- 836 [Dataset] A-SAIL Project (2020). A-sail project. [https://www.qub.ac.uk/  
837 research-centres/A-SAILProject/](https://www.qub.ac.uk/research-centres/A-SAILProject/)
- 838 Amin, T., Barlow, R., Ghithan, S., Royb, G., and Schuhb, S. (2018). Formation of a uniform ion beam  
839 using octupole magnets for bioleir facility at cern. *JINST* 13, P04016
- 840 Atun, R., Jaffray, D. A., Barton, M. B., Bray, F., Baumann, M., Vikram, B., et al. (2015). Expanding  
841 global access to radiotherapy. *The Lancet Oncology* 16, 1153 – 1186. doi:[https://doi.org/10.1016/  
842 S1470-2045\(15\)00222-3](https://doi.org/10.1016/S1470-2045(15)00222-3)
- 843 Autin, B., Carli, C., D'Amico, T., Gröbner, O., Martini, M., and Wildner, E. (1998). *BeamOptics:*  
844 *A program for analytical beam optics*. Tech. Rep. CERN–98-06, European Organization for  
845 Nuclear Research (CERN). [http://inis.iaea.org/search/search.aspx?orig\\_q=RN:  
846 30052986](http://inis.iaea.org/search/search.aspx?orig_q=RN:30052986)
- 847 Barber, G. (2018). Outline design and cost estimate for the SmartPhantom. *Unpublished note*
- 848 Bin, J., Allinger, K., Assmann, W., Dollinger, G., Drexler, G. A., Friedl, A. A., et al. (2012). A laser-  
849 driven nanosecond proton source for radiobiological studies. *Applied Physics Letters* 101, 243701.  
850 doi:10.1063/1.4769372
- 851 Bin, J., Ma, W., Wang, H., Streeter, M., Kreuzer, C., Kiefer, D., et al. (2015). Ion Acceleration Using  
852 Relativistic Pulse Shaping in Near-Critical-Density Plasmas. *Physical Review Letters* 115, 064801.  
853 doi:10.1103/PhysRevLett.115.064801
- 854 Bray, F., Ferlay, J., Soerjomataram, I., Siegel, R. L., Torre, L. A., and Jemal, A. (2018). Global cancer  
855 statistics 2018: GLOBOCAN estimates of incidence and mortality worldwide for 36 cancers in 185  
856 countries. *CA: A Cancer Journal for Clinicians* 68, 394–424. doi:10.3322/caac.21492
- 857 Bulanov, S., Esirkepov, T., Khoroshkov, V., Kuznetsov, A., and Pegoraro, F. (2002). Oncological  
858 hadrontherapy with laser ion accelerators. *Physics Letters A* 299, 240–247. doi:[https://doi.org/10.1016/  
859 S0375-9601\(02\)00521-2](https://doi.org/10.1016/S0375-9601(02)00521-2)
- 860 Carter, R. J., Nickson, C. M., Thompson, J. M., Kacpersek, A., Hill, M. A., and Parsons, J. L. (2018).  
861 Complex dna damage induced by high linear energy transfer alpha-particles and protons triggers a  
862 specific cellular dna damage response. *International Journal of Radiation Oncology\*Biophysics*  
863 100, 776 – 784. doi:<https://doi.org/10.1016/j.ijrobp.2017.11.012>
- 864 Chaudhary, P., Gwynne, D., Doria, D., Romagnani, L., Maiorino, C., Padda, H., et al. (2017). Effectiveness  
865 of laser accelerated ultra high dose rate protons in DNA DSB damage induction under hypoxic conditions.  
866 In *44th EPS Conference on Plasma Physics, EPS 2017* (European Physical Society (EPS)), vol. 44F.  
867 P1.217
- 868 Chaudhary, P., Marshall, T. I., Perozziello, F. M., Manti, L., Currell, F. J., Hanton, F., et al. (2014). Relative  
869 Biological Effectiveness Variation Along Monoenergetic and Modulated Bragg Peaks of a 62-MeV  
870 Therapeutic Proton Beam: A Preclinical Assessment. *International Journal of Radiation Oncology •  
871 Biology • Physics* 90, 27–35. doi:10.1016/j.ijrobp.2014.05.010
- 872 Chen, S. N., Vranic, M., Gangolf, T., Boella, E., Antici, P., Bailly-Grandvaux, M., et al. (2017). Collimated  
873 protons accelerated from an overdense gas jet irradiated by a 1  $\mu\text{m}$  wavelength high-intensity short-pulse  
874 laser. *Scientific Reports* 7, 13505. doi:10.1038/s41598-017-12910-6

- 875 Cirrone, G., Catalano, R., Cuttone, G., Margarone, D., Schillaci, F., and Petringa, G. (2020). Generation  
876 control and application of flash radiation beam from laser-matter interaction: The ELIMAIA-ELIMED  
877 beamline. *Nuovo Cim. C* 43, 15. doi:10.1393/ncc/i2020-20015-6
- 878 Cirrone, G. et al. (2016). Status, Plans and Potential Applications of the ELIMED Beam Line at  
879 ELI-Beamlines. In *7th International Particle Accelerator Conference*. WEXB01. doi:10.18429/  
880 JACoW-IPAC2016-WEXB01
- 881 Cirrone, G. A. P., Margarone, D., Maggiore, M., Anzalone, A., Borghesi, M., Jia, S. B., et al. (2013).  
882 ELIMED: a new hadron therapy concept based on laser driven ion beams. In *Laser Acceleration of*  
883 *Electrons, Protons, and Ions II; and Medical Applications of Laser-Generated Beams of Particles II;*  
884 *and Harnessing Relativistic Plasma Waves III*, eds. E. Esarey, C. B. Schroeder, W. P. Leemans, K. W. D.  
885 Ledingham, and D. A. Jaroszynski. International Society for Optics and Photonics (SPIE), vol. 8779,  
886 216 – 225. doi:10.1117/12.2026530
- 887 Clark, E. L., Krushelnick, K., Davies, J. R., Zepf, M., Tatarakis, M., Beg, F. N., et al. (2000a).  
888 Measurements of energetic proton transport through magnetized plasma from intense laser interactions  
889 with solids. *Phys. Rev. Lett.* 84, 670–673. doi:10.1103/PhysRevLett.84.670
- 890 Clark, E. L., Krushelnick, K., Zepf, M., Beg, F. N., Tatarakis, M., Machacek, A., et al. (2000b). Energetic  
891 heavy-ion and proton generation from ultraintense laser-plasma interactions with solids. *Phys. Rev. Lett.*  
892 85, 1654–1657. doi:10.1103/PhysRevLett.85.1654
- 893 Daido, H., Nishiuchi, M., and Pirozhkov, A. S. (2012). Review of laser-driven ion sources and their  
894 applications. *Reports on Progress in Physics* 75, 56401. doi:10.1088/0034-4885/75/5/056401
- 895 Datta, N. R., Rogers, S., and Bodis, S. (2019). Challenges and Opportunities to Realize “The 2030 Agenda  
896 for Sustainable Development” by the United Nations: Implications for Radiation Therapy Infrastructure  
897 in Low- and Middle-Income Countries. *International Journal of Radiation Oncology\*Biophysics\*Physics*  
898 105, 918–933. doi:https://doi.org/10.1016/j.ijrobp.2019.04.033
- 899 De Loos, M. J. and Van der Geer, S. B. (1996). General Particle Tracer: A New 3D Code for Accelerator  
900 and Beamline Design
- 901 deGrassie, J. S. and Malmberg, J. H. (1980). Waves and transport in the pure electron plasma. *The Physics*  
902 *of Fluids* 23, 63–81. doi:10.1063/1.862864
- 903 Doria, D., Kakolee, K. F., Kar, S., Litt, S. K., Fiorini, F., Ahmed, H., et al. (2012). Biological effectiveness  
904 on live cells of laser driven protons at dose rates exceeding  $10^9$  Gy/s. *AIP Advances* 2, 011209.  
905 doi:10.1063/1.3699063
- 906 Dover, N., Nishiuchi, M., Sakaki, H., Kondo, K., Lowe, H., Alkhimova, M., et al. (2020). Demonstration  
907 of repetitive energetic proton generation by ultra-intense laser interaction with a tape target. *High Energy*  
908 *Density Physics* 37, 100847. doi:10.1016/j.hedp.2020.100847
- 909 Favaudon, V., Caplier, L., Monceau, V., Pouzoulet, F., Sayarath, M., Fouillade, C., et al. (2014). Ultrahigh  
910 dose-rate flash irradiation increases the differential response between normal and tumor tissue in mice.  
911 *Science Translational Medicine* 6, 245ra93–245ra93. doi:10.1126/scitranslmed.3008973
- 912 Fiorini, F., Kirby, D., Borghesi, M., Doria, D., Jeynes, J. C., Kakolee, K. F., et al. (2011). Dosimetry and  
913 spectral analysis of a radiobiological experiment using laser-driven proton beams. *Phys Med Biol* 56,  
914 6969–6982
- 915 Fitzmaurice, C., Akinyemiju, T. F., Al Lami, F. H., Alam, T., Alizadeh-Navaei, R., Allen, C., et al. (2018).  
916 Global, Regional, and National Cancer Incidence, Mortality, Years of Life Lost, Years Lived With  
917 Disability, and Disability-Adjusted Life-Years for 29 Cancer Groups, 1990 to 2016. *JAMA Oncology* 4,  
918 1553. doi:10.1001/jamaoncol.2018.2706

- 919 Fourkal, E., Li, J. S., Ding, M., Tajima, T., and Ma, C. M. (2003). Particle selection for laser-accelerated  
920 proton therapy feasibility study. *Medical Physics* 30, 1660–1670. doi:10.1118/1.1586268
- 921 Fourier, J., Martinache, F., Meot, F., and Pasternak, J. (2008). Spiral ftag lattice design tools. application  
922 to 6-d tracking in a proton-therapy class lattice. *Nucl. Instrum. Meth. A* 589, 133–142. doi:10.1016/j.  
923 nima.2008.01.082
- 924 Gabor, D. (1947). A Space-Charge Lens for the Focusing of Ion Beams. *Nature* 160, 89–90. doi:10.1038/  
925 160089b0
- 926 Gauthier, M., Curry, C. B., Göde, S., Brack, F.-E., Kim, J. B., MacDonald, M. J., et al. (2017). High  
927 repetition rate, multi-mev proton source from cryogenic hydrogen jets. *Applied Physics Letters* 111,  
928 114102. doi:10.1063/1.4990487
- 929 Grote, H. and Schmidt, F. (2003). MAD-X: An upgrade from MAD8. *Conf. Proc. C* 030512, 3497
- 930 HSE (2018). *Work with ionising radiation - Ionising Radiations Regulations 2017* (Crown)
- 931 Karger, C. P. and Peschke, P. (2017). RBE and related modeling in carbon-ion therapy. *Physics in Medicine  
932 & Biology* 63, 01TR02. doi:10.1088/1361-6560/aa9102
- 933 Kraft, S. D., Richter, C., Zeil, K., Baumann, M., Beyreuther, E., Bock, S., et al. (2010). Dose-dependent  
934 biological damage of tumour cells by laser-accelerated proton beams. *New Journal of Physics* 12, 85003.  
935 doi:10.1088/1367-2630/12/8/085003
- 936 Krest, D., Laslett, L., Jones, L. W., Symon, K., and Terwilliger, K. (1956). *Fixed field alternating gradient  
937 particle accelerators*. Tech. Rep. MURA-109, MURA-DWK-KRS-LJL-LWJ-KMT-3, Midwestern  
938 Universities Research Association (MURA)
- 939 Kurup, A. (2019). Diagnostics for LhARA. *Low energy ion beam diagnostics workshop, Imperial College*
- 940 Lagrange, J. B., Appleby, R. B., Garland, J. M., Pasternak, J., and Tygier, S. (2018). Racetrack FFAG  
941 muon decay ring for nuSTORM with triplet focusing. *JINST* 13, P09013. doi:10.1088/1748-0221/13/  
942 09/P09013
- 943 Letchford, A. et al. (2015). Status of the ral front end test stand. In *IPAC*
- 944 Loeffler, J. S. and Durante, M. (2013). Charged particle therapy—optimization, challenges and future  
945 directions. *Nature Reviews Clinical Oncology* 10, 411–424. doi:10.1038/nrclinonc.2013.79
- 946 Malka, V., Fritzler, S., Lefebvre, E., d’Humières, E., Ferrand, R., Grillon, G., et al. (2004). Practicability of  
947 proton therapy using compact laser systems. *Medical Physics* 31, 1587–1592. doi:10.1118/1.1747751
- 948 Malmberg, J. H., Driscoll, C. F., Beck, B., Eggleston, D. L., Fajans, J., Fine, K., et al. (1988). Experiments  
949 with pure electron plasmas. *AIP Conference Proceedings* 175, 28–74. doi:10.1063/1.37613
- 950 Manti, L., Perozziello, F. M., Borghesi, M., Candiano, G., Chaudhary, P., Cirrone, G. A., et al. (2017).  
951 The radiobiology of laser-driven particle beams: Focus on sub-lethal responses of normal human cells.  
952 *Journal of Instrumentation* 12. doi:10.1088/1748-0221/12/03/C03084
- 953 Margarone, D., Cirrone, G. A. P., Cuttone, G., Amico, A., Andò, L., Borghesi, M., et al. (2018).  
954 Elimaia: A laser-driven ion accelerator for multidisciplinary applications. *Quantum Beam Science* 2.  
955 doi:10.3390/qubs2020008
- 956 Margarone, D., Velyhan, A., Dostal, J., Ullschmied, J., Perin, J. P., Chatain, D., et al. (2016). Proton  
957 acceleration driven by a nanosecond laser from a cryogenic thin solid-hydrogen ribbon. *Phys. Rev. X* 6,  
958 041030. doi:10.1103/PhysRevX.6.041030
- 959 Masood, U., Bussmann, M., Cowan, T. E., Enghardt, W., Karsch, L., Kroll, F., et al. (2014). A  
960 compact solution for ion beam therapy with laser accelerated protons. *Applied Physics B* 117, 41–52.  
961 doi:https://doi.org/10.1007/s00340-014-5796-z
- 962 Masood, U., Cowan, T. E., Enghardt, W., Hofmann, K. M., Karsch, L., Kroll, F., et al. (2017). A  
963 light-weight compact proton gantry design with a novel dose delivery system for broad-energetic

- 964 laser-accelerated beams. *Physics in Medicine & Biology* 62, 5531–5555. doi:10.1088/1361-6560/aa7124
- 965 Meusel, O., Droba, M., Glaeser, B., and Schulte, K. (2013). Experimental studies of stable confined electron
- 966 clouds using Gabor lenses. *Conf. Proc. C* 1206051, 157–160. doi:10.5170/CERN-2013-002.157
- 967 Milluzzo, G. et al. (2017). Laser-accelerated ion beam diagnostics with TOF detectors for the ELIMED
- 968 beam line. *JINST* 12, C02025. doi:10.1088/1748-0221/12/02/C02025
- 969 Milluzzo, G. et al. (2018). Geant4 simulation of the ELIMED transport and dosimetry beam line for
- 970 high-energy laser-driven ion beam multidisciplinary applications. *Nucl. Instrum. Meth. A* 909, 298–302.
- 971 doi:10.1016/j.nima.2018.02.066
- 972 Morrison, J. T., Feister, S., Frische, K. D., Austin, D. R., Ngirmang, G. K., Murphy, N. R., et al. (2018).
- 973 MeV proton acceleration at kHz repetition rate from ultra-intense laser liquid interaction. *New Journal*
- 974 *of Physics* 20, 22001. doi:10.1088/1367-2630/aaa8d1
- 975 Nevay, L. J. et al. (2020). Bdsim: An accelerator tracking code with particle-matter interactions. *Computer*
- 976 *Physics Communications* , 107200
- 977 NIST (2017). *NIST Standard Reference Database 124* (National Institute of Standards and Technology).
- 978 doi:https://dx.doi.org/10.18434/T4NC7P
- 979 Noaman-ul Haq, M., Ahmed, H., Sokollik, T., Yu, L., Liu, Z., Yuan, X., et al. (2017). Statistical analysis of
- 980 laser driven protons using a high-repetition-rate tape drive target system. *Phys. Rev. Accel. Beams* 20,
- 981 041301. doi:10.1103/PhysRevAccelBeams.20.041301
- 982 Obst, L., Göde, S., Rehwald, M., Brack, F.-E., Branco, J., Bock, S., et al. (2017). Efficient laser-driven
- 983 proton acceleration from cylindrical and planar cryogenic hydrogen jets. *Scientific Reports* 7, 10248.
- 984 doi:10.1038/s41598-017-10589-3
- 985 Paganetti, H. (2014). Relative biological effectiveness (RBE) values for proton beam therapy. Variations as
- 986 a function of biological endpoint, dose, and linear energy transfer. *Phys. Med. Biol.* 59, R419
- 987 Paganetti, H. and van Luijk, P. (2013). Biological considerations when comparing proton therapy with
- 988 photon therapy. *Seminars in Radiation Oncology* 23, 77 – 87. doi:https://doi.org/10.1016/j.semradonc.
- 989 2012.11.002. Controversies in Proton Therapy
- 990 Passoni, M., Bertagna, L., and Zani, A. (2010). Target normal sheath acceleration: theory, comparison with
- 991 experiments and future perspectives. *New Journal of Physics* 12, 045012. doi:10.1088/1367-2630/12/4/
- 992 045012
- 993 Pipek, J. et al. (2017). Monte Carlo simulation of the ELIMED beamline using Geant4. *JINST* 12, C03027.
- 994 doi:10.1088/1748-0221/12/03/C03027
- 995 Planche, T., Fourrier, J., Lancelot, J. L., Meot, F., Neuveglise, D., and Pasternak, J. (2009). Design of a
- 996 prototype gap shaping spiral dipole for a variable energy protontherapy FFAG. *Nucl. Instrum. Meth.*
- 997 *A*604, 435–442. doi:10.1016/j.nima.2009.02.026
- 998 Pommarel, L., Vauzour, B., Mégnin-Chanet, F., Bayart, E., Delmas, O., Goudjil, F., et al. (2017). Spectral
- 999 and spatial shaping of a laser-produced ion beam for radiation-biology experiments. *Physical Review*
- 1000 *Accelerators and Beams* 20, 1–10. doi:10.1103/PhysRevAccelBeams.20.032801
- 1001 Pozimski, J. and Aslaninejad, M. (2013). Gabor lenses for capture and energy selection of laser driven ion
- 1002 beams in cancer treatment. *Laser and Particle Beams* 31, 723—733. doi:10.1017/S0263034613000761
- 1003 Prezado, Y., Jouvion, G., Hardy, D., Patriarca, A., Nauraye, C., Bergs, J., et al. (2017). Proton minibeam
- 1004 radiation therapy spares normal rat brain: Long-Term Clinical, Radiological and Histopathological
- 1005 Analysis. *Scientific Reports* 7, 14403. doi:10.1038/s41598-017-14786-y
- 1006 [Dataset] PTCOG (2020). Particle Therapy Co-Operative Group. [https://www.ptcog.ch/index.](https://www.ptcog.ch/index.php/patient-statistics)
- 1007 [php/patient-statistics](https://www.ptcog.ch/index.php/patient-statistics)

- 1008 Reiser, M. (1989). Comparison of gabor lens, gas focusing, and electrostatic quadrupole focusing for  
1009 low-energy ion beams. In *Proceedings of the 1989 IEEE Particle Accelerator Conference*, . 'Accelerator  
1010 *Science and Technology*. 1744–1747 vol.3
- 1011 Romano, F., Schillaci, F., Cirrone, G., Cuttone, G., Scuderi, V., Allegra, L., et al. (2016a). The elimed  
1012 transport and dosimetry beamline for laser-driven ion beams. *Nuclear Instruments and Methods in*  
1013 *Physics Research Section A: Accelerators, Spectrometers, Detectors and Associated Equipment* 829,  
1014 153–158. doi:<https://doi.org/10.1016/j.nima.2016.01.064>. 2nd European Advanced Accelerator Concepts  
1015 Workshop – EAAC 2015
- 1016 Romano, F. et al. (2016b). The ELIMED transport and dosimetry beamline for laser-driven ion beams.  
1017 *Nucl. Instrum. Meth. A* 829, 153–158. doi:10.1016/j.nima.2016.01.064
- 1018 Schillaci, F. et al. (2019). Advanced Beam Transport Solutions for ELIMAIA: A User Oriented Laser-  
1019 Driven Ion Beamlines. In *10th International Particle Accelerator Conference*. TUPTS005. doi:10.  
1020 18429/JACoW-IPAC2019-TUPTS005
- 1021 Snavely, R. A., Key, M. H., Hatchett, S. P., Cowan, T. E., Roth, M., Phillips, T. W., et al. (2000). Intense  
1022 high-energy proton beams from petawatt-laser irradiation of solids. *Phys. Rev. Lett.* 85, 2945–2948.  
1023 doi:10.1103/PhysRevLett.85.2945
- 1024 [Dataset] STFC (2019a). The astra gemini facility. [https://www.clf.stfc.ac.uk/Pages/  
1025 The-Astra-Gemini-Facility.aspx](https://www.clf.stfc.ac.uk/Pages/The-Astra-Gemini-Facility.aspx)
- 1026 [Dataset] STFC (2019b). Introducing the extreme photonics applications centre. [https://www.clf.  
1027 stfc.ac.uk/Pages/EPAC-introduction-page.aspx](https://www.clf.stfc.ac.uk/Pages/EPAC-introduction-page.aspx)
- 1028 [Dataset] STFC (2019c). Isis neutron and muon source. [https://stfc.ukri.org/research/  
1029 our-science-facilities/isis-neutron-and-muon-source/](https://stfc.ukri.org/research/our-science-facilities/isis-neutron-and-muon-source/)
- 1030 Symon, K. R., Kerst, D. W., Jones, L. W., Laslett, L. J., and Terwilliger, K. M. (1956). Fixed-field  
1031 alternating-gradient particle accelerators. *Phys. Rev.* 103, 1837–1859. doi:10.1103/PhysRev.103.1837
- 1032 Tanigaki, M., Mori, Y., Inoue, M., Mishima, K., Shiroya, S., Ishi, Y., et al. (2006). Present status of the  
1033 ftag accelerators in kurri for ads study. In *EPAC 2006 - Contributions to the Proceedings*
- 1034 The LhARA consortium (2020). *The Laser-hybrid Accelerator for Radiobiological Applications*.  
1035 Tech. Rep. CCAP-TN-01. [https://ccap.hep.ph.ic.ac.uk/trac/raw-attachment/  
1036 wiki/Research/DesignStudy/PreCDR/Review/2020-03-31-LhARA\\_pre\\_CDR-d2.  
1037 0.pdf](https://ccap.hep.ph.ic.ac.uk/trac/raw-attachment/wiki/Research/DesignStudy/PreCDR/Review/2020-03-31-LhARA_pre_CDR-d2.0.pdf)
- 1038 [Dataset] The World Health Organisation (2020). Cancer. [https://www.who.int/news-room/  
1039 fact-sheets/detail/cancer](https://www.who.int/news-room/fact-sheets/detail/cancer)
- 1040 Thompson, R. C. (2015). PENNING TRAPS. In *Trapped Charged Particles* (WORLD SCIENTIFIC  
1041 (EUROPE)), Advanced Textbooks in Physics. 1–33. doi:doi:10.1142/9781786340139\_0001
- 1042 Tsoupas, N. et al. (1991). Uniform beam distributions using octupoles. *Proceedings of PAC 1991* ,  
1043 1695–1697
- 1044 Uesugi, T. (2018). Betatron Tune Measurement . *FFA School, Osaka*
- 1045 Urakabe, E. et al. (1999). Beam-profile control using an octupole magnet. *Jpn. J. Appl. Phys.* 38,  
1046 6145–6149
- 1047 Vitti, E. T. and Parsons, J. L. (2019). The radiobiological effects of proton beam therapy: Impact on dna  
1048 damage and repair. *Cancers* 11. doi:10.3390/cancers11070946
- 1049 Vozenin, M. C., De Fornel, P., Petersson, K., Favaudon, V., Jaccard, M., Germond, J. F., et al. (2019). The  
1050 Advantage of FLASH Radiotherapy Confirmed in Mini-pig and Cat-cancer Patients. *Clin. Cancer Res.*  
1051 25, 35–42. doi:10.1158/1078-0432

- 1052 Wang, H. (2014). Wavefront measurement techniques used in high power lasers. *High Power Laser Science*  
1053 *and Engineering* 2
- 1054 Wiggins, S. M., Boyd, M., Brunetti, E., Butler, N. M. H., Feehan, J. S., Gray, R. J., et al. (2019). Application  
1055 programmes at the Scottish Centre for the Application of Plasma-based Accelerators (SCAPA). In  
1056 *Relativistic Plasma Waves and Particle Beams as Coherent and Incoherent Radiation Sources III*, eds.  
1057 D. A. Jaroszynski and M. Hur. International Society for Optics and Photonics (SPIE), vol. 11036, 93 –  
1058 103. doi:10.1117/12.2520717
- 1059 Wilkens, J. J. and Oelfke, U. (2004). A phenomenological model for the relative biological effectiveness in  
1060 therapeutic proton beams. *Physics in Medicine and Biology* 49, 2811–2825. doi:10.1088/0031-9155/49/  
1061 13/004
- 1062 Willingale, L., Nagel, S. R., Thomas, A. G. R., Bellei, C., Clarke, R. J., Dangor, A. E., et al. (2009).  
1063 Characterization of High-Intensity Laser Propagation in the Relativistic Transparent Regime through  
1064 Measurements of Energetic Proton Beams. *Physical Review Letters* 102, 125002. doi:10.1103/  
1065 PhysRevLett.102.125002
- 1066 Yogo, A., Maeda, T., Hori, T., Sakaki, H., Ogura, K., Nishiuchi, M., et al. (2011). Measurement of relative  
1067 biological effectiveness of protons in human cancer cells using a laser-driven quasimonoenergetic proton  
1068 beamline. *Applied Physics Letters* 98, 053701. doi:10.1063/1.3551623
- 1069 Yonemura, Y., Arima, H., Ikeda, N., Ishibashi, K., Maehata, K., Noro, T., et al. (2008). Status of center  
1070 for accelerator and beam applied science of kyushu university. *EPAC 2008 - Contributions to the*  
1071 *Proceedings*
- 1072 Zeil, K., Baumann, M., Beyreuther, E., Burris-Mog, T., Cowan, T. E., Enghardt, W., et al. (2013).  
1073 Dose-controlled irradiation of cancer cells with laser-accelerated proton pulses. *Applied Physics B* 110,  
1074 437–444. doi:10.1007/s00340-012-5275-3
- 1075 Zlobinskaya, O., Siebenwirth, C., Greubel, C., Hable, V., Hertenberger, R., Humble, N., et al. (2014).  
1076 The effects of ultra-high dose rate proton irradiation on growth delay in the treatment of human tumor  
1077 xenografts in nude mice. *Radiation Research* 181, 177–183. doi:10.1667/RR13464.1